CellPress
OPEN ACCESS

Article

Morphogenesis and oxygen dynamics in phototrophic biofilms growing across a gradient of hydraulic conditions

Phototrophic biofilms

Low bed shear stress   High bed shear stress

Optical coherence tomography

O₂ microprofiling   Fluid dynamics simulation

Anna Depetris,
Hannes Peter,
Ankur Deep
Bordoloi, ...,
Michael Kühl,
Pietro de Anna,
Tom Jan Battin

tom.battin@epfl.ch

HIGHLIGHTS
We explored the structural
differentiation of
phototrophic biofilms in
flume experiments

Two distinct
morphologies emerged
depending on bed shear
stress

Oxygen measurements
suggest efficient mass
transfer in both
morphologies

Feedbacks between
structure and hydraulics
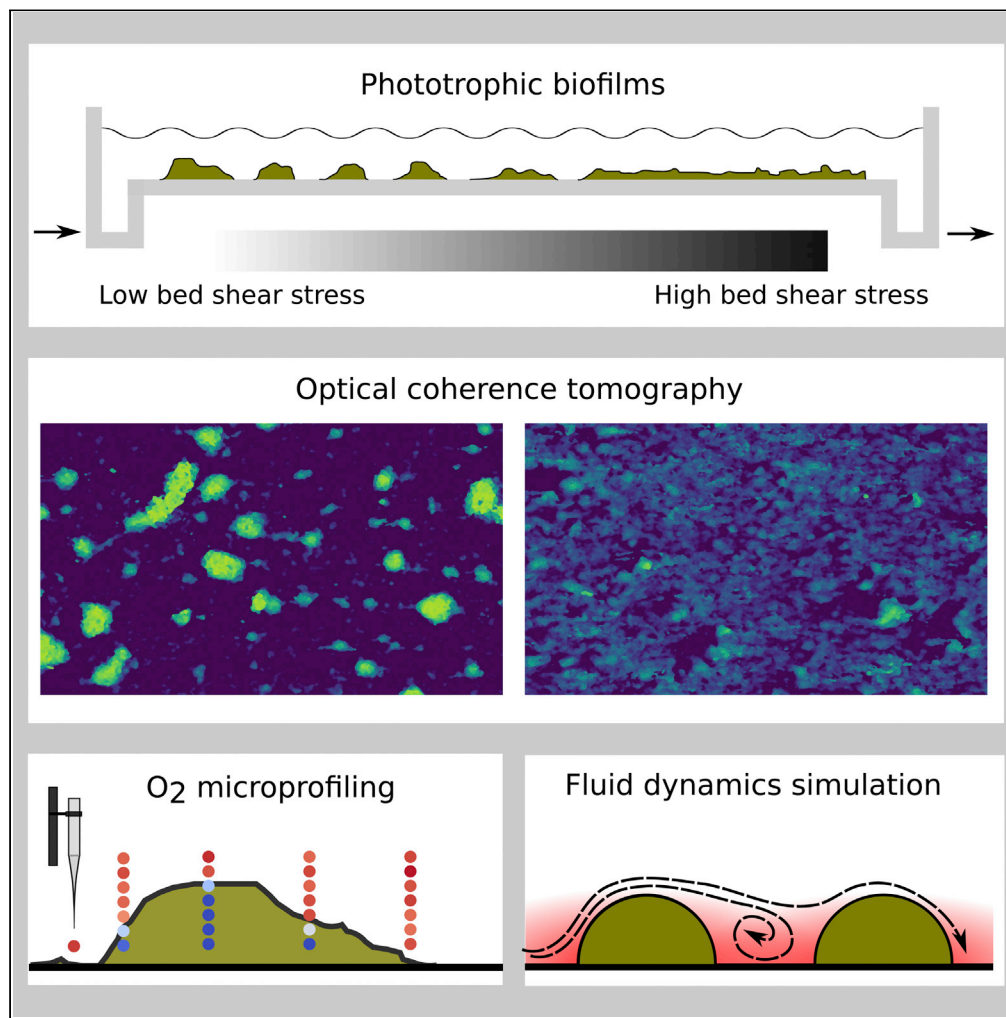drive biofilm
morphogenesis

Article

Morphogenesis and oxygen dynamics in phototrophic biofilms growing across a gradient of hydraulic conditions

Anna Depetris,[1] Hannes Peter,[1] Ankur Deep Bordoloi,[2] Hippolyte Bernard,[1] Amin Niayifar,[1] Michael Kühl,[3] Pietro de Anna,[2] and Tom Jan Battin[1,4,*]

SUMMARY

Biofilms are surface-attached and matrix-enclosed microbial communities that dominate microbial life in numerous ecosystems. Using flumes and automated optical coherence tomography, we studied the morphogenesis of phototrophic biofilms along a gradient of hydraulic conditions. Compact and coalescent biofilms formed under elevated bed shear stress, whereas protruding clusters separated by troughs formed under reduced shear stress. This morphological differentiation did not linearly follow the hydraulic gradient, but a break point emerged around a shear stress of ~0.08 Pa. While community composition did not differ between high and low shear environments, our results suggest that the morphological differentiation was linked to biomass displacement and reciprocal interactions between the biofilm structure and hydraulics. Mapping oxygen concentrations within and around biofilm structures, we provide empirical evidence for biofilm-induced alterations of oxygen mass transfer. Our findings suggest that architectural plasticity, efficient mass transfer, and resistance to shear stress contribute to the success of phototrophic biofilms.

INTRODUCTION

Microorganisms form surface-attached and matrix-enclosed biofilms in numerous ecosystems (Flemming and Wuertz, 2019). A conspicuous and ubiquitous feature of biofilms is the differentiation into physical structures (*i.e.*, architectures) and the formation of spatial patterns and stratifications at various scales. Despite the importance of spatial organization for ecological systems in general (Rietkerk, 2004), relatively little is known on the formation of the higher-order structures in complex biofilms. This is unexpected given that biofilm architecture seems to be related to critical processes in many benthic ecosystems (Battin et al., 2016; Findlay and Battin, 2016).

The study of the diverse physical structures of biofilms has been a mainstay in biofilm research. Reported architectures include cell clusters separated by voids (De Beer et al., 1994, 1996; Stoodley et al., 2001, 2002), mushroom-like caps, streamers extending into the bulk liquid (Hall-Stoodley et al., 2004; Stoodley et al., 2002), ripples (Neu and Lawrence, 2006; Stoodley et al., 1999), and honeycomb-like patterns (Battin et al., 2003; Guilbaud et al., 2015; Thar and Kühl, 2005). Redox balancing, mechanical instabilities, reciprocal interactions between growth and competition for nutrients, localized cell death, and grazing by protists have been invoked as endogenous drivers of biofilm morphogenesis (Xavier et al., 2009; Yan et al., 2019; Dietrich et al., 2013; Weitere et al., 2018).

The bed shear stress imposed by fluid flow is an important exogenous driver of biofilm structural differentiation. It can trigger sloughing and deformation of biofilms (Drescher et al., 2016; Stewart, 2012; Stoodley et al., 2001), or the formation of patterns such as migratory ripples (Stoodley et al., 1999). While dense and compact biofilms are better protected from shear stress and related drag fluid (Sudarsan et al., 2016; Wang et al., 2018), tall and exposed clusters are more susceptible to sloughing or displacement (Dunsmore et al., 2002). Furthermore, the production of extracellular polymeric substances (EPSs) can be modulated in response to high shear, conferring enhanced mechanical stability (Battin et al., 2003; Simões et al., 2007; Wang et al., 2014). Fluid flow also affects the thickness of the diffusive boundary layer, the establishment of chemical gradients and thereby resource replenishment and biofilm growth (Battin et al., 2003; Hondzo

[1]Stream Biofilm and Ecosystem Research Laboratory, School of Architecture, Civil and Environmental Engineering, École polytechnique fédérale de Lausanne, 1015 Lausanne, Switzerland

[2]Institute of Earth Sciences, University of Lausanne, 1015 Lausanne, Switzerland

[3]Marine Biological Section, Department of Biology, University of Copenhagen, Strandpromenaden 5, 3000 Helsingør, Denmark

[4]Lead contact

*Correspondence: tom.battin@epfl.ch

https://doi.org/10.1016/j.isci.2021.102067

and Wang, 2002; Park et al., 2011; Picioreanu et al., 2009; Stewart, 2012; Stewart and Franklin, 2008; Stoodley et al., 1998). Thus, the link between fluid flow and both biofilm growth and structure is complex, influenced between the balance between shear-induced biomass loss and enhanced mass transfer and growth rate (Park et al., 2011; Simões et al., 2007; Hondzo and Wang, 2002; Wang et al., 2014). At the same time, biofilm architecture can also modify the local flow patterns. In fact, mathematical models and experiments have shown that troughs between adjacent clusters alter the flow fields around the latter, allowing for fluid flow around the basal layers of the biofilm, thereby enhancing mass transport to these otherwise nutrient-limited areas (De Beer et al., 1994; Picioreanu et al., 2000). Therefore, like in macroscopic landscapes such as coral reefs or forests, the structure of biofilms mediates in the biogenic construction of its immediate environment (Flemming et al., 2016).

Our current understanding of biofilm morphogenesis and patterning largely rests on mathematical modeling. For instance, external mass transfer resistance imposed by a thick diffusive boundary layer may be counteracted by the formation of finger-like and rough biofilm architectures (e.g., Van Loosdrecht et al., 2002; Picioreanu et al., 1998). Here, models have shown that tall and exposed clusters grow faster than smaller clusters because they access more of the limiting resource (e.g., nutrients, oxygen) in the bulk fluid. Local detachment can also influence biofilm morphogenesis. The erosion of structures protruding into the fluid flow may result in biofilms with low roughness, while sloughing, as linked to nutrient limitation at the biofilm base or the erosion of cells from the biofilm surface, can lead to rough and clumped architectures (Chambless and Stewart, 2007; Hunt et al., 2004).

Such modeling efforts have influenced experimental studies on biofilm formation and morphogenesis that, however, remain often limited to mono-species bacterial biofilms growing on agar plates or in flow cells (e.g., Bjarnsholt et al., 2013; Rossy et al., 2019). While such experiments have greatly advanced our understanding on the small-scale architecture of biofilms and interactions within them, they may poorly reflect the impact of complex fluid flow on biofilm morphogenesis and its characteristic length scale as often encountered in natural biofilm habitats, such as streams. In fact, complex biofilms, whether in stream ecosystems (Battin et al., 2016) or the intestine (Cremer et al., 2016), are often characterized by spatial patterns that exceed the dimensions of a typical flow cell. Approaches that provide high spatial resolution beyond the multi-millimeter scale are thus required to appreciate the governing physical, biological and ecological processes from which architectures and higher-order patterns emerge (Battin et al., 2007; Dzubakova et al., 2018; Milferstedt et al., 2009; Wagner et al., 2010; Yan et al., 2019).

Here we applied an experimental and multi-scale approach to relate the structure and function of phototrophic biofilms to their hydraulic environment. We used an automated optical coherence tomography (OCT) system (Depetris et al., 2019) to quantify the topography of the biofilm as a digital elevation model (DEM) over a large rectangular surface (0.025 m × 0.4 m). This approach is analogous to the *in situ* 3D imaging of forests and coral reefs providing quantitative and detailed structural information to test hypotheses relating structure to function of these ecosystems (Calders et al., 2020). Biofilms grew in experimental flumes along an increasing gradient of flow velocity and shear stress. Our general hypothesis was that differing space-occupancy strategies arise from trade-offs between flow-induced shear stress and nutrient replenishment, thereby resulting in a patterned microbial landscape. Guided by numerical simulations of flow across idealized biofilm structures and oxygen concentration microprofiles, we further show that biofilm structures are able to modify their local environment.

RESULTS AND DISCUSSION

Hydraulics affects biofilm architecture and patterning

We cultivated phototrophic biofilms from raw water from Lake Geneva to mimic their growth in the lake outlet, the Rhone River. Biofilms grew over 15 days in duplicate open-channel flumes (I and II, 1.5 m long) with a geometry designed to produce a hydraulic gradient (Figures 1A and S1). Along this gradient, mean flow velocity ranged from 0.06 m s^{-1} to 0.13 m s^{-1}, and Reynolds number for open channel flow (Supplemental information) increased from 793 to 1407, indicative of laminar to transitional flow, respectively. Numerical simulations further showed that the bed shear stress increased from 0.04 Pa to 0.13 Pa (Figure 1B). We used an automated OCT system (Depetris et al., 2019) to characterize the biofilm surface topology at high resolution (40 μm, 40 μm, and 2.18 μm in x, y, z dimensions) across several spatial scales — ranging from patches formed by multicellular clusters (~100 μm) to the higher-order patterns emerging at the scale of the entire biofilm landscape (0.4 m in length) (Figures 1C–1G). The OCT scans did not evidence
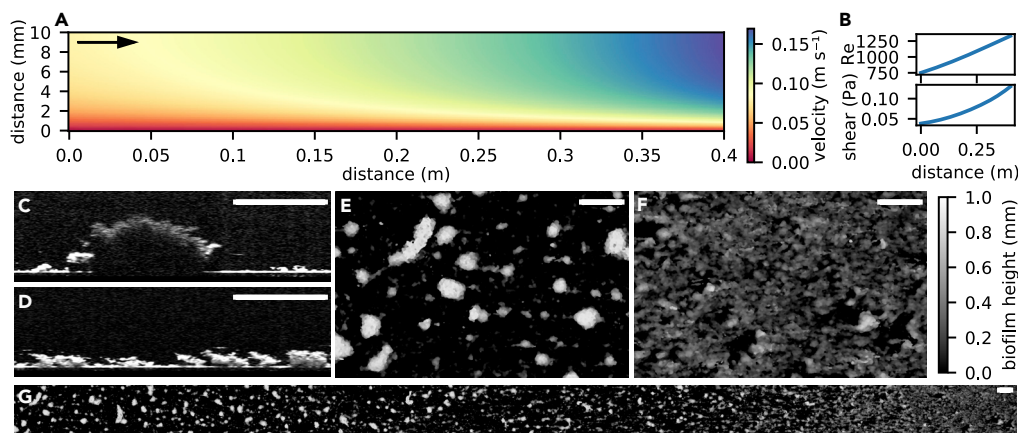
Figure 1. Architectural differentiation of phototrophic biofilms follows the hydraulic gradient

The narrowing flume design from inlet to outlet (Figure S1) resulted in a gradual increase in flow velocity and bed shear stress in flow direction. An axial cross-section of the simulated velocity field is shown (A), with distance in the flow direction and from the flume bed on the x and y axes, respectively. Reynolds numbers and bed shear stress also increased in the flow direction (B) Optical coherence tomography (OCT) produced stacks of cross-sections at high resolution. Representative scans are shown for low (C) and high shear regions (D). OCT scans were processed to quantify the biofilm surface topology as a digital elevation models (DEM), in which biofilm thickness is encoded as pixel gray-level. Shown is a DEM covering a rectangle of 0.025×0.4 m^2 along the hydraulic gradient (G), while enlarged details of the biofilm developed under low-shear (SFM) and high-shear (FFM) are also reported (E; F, respectively). Scale bars: 5 mm. Flow direction for all panels is indicated by the arrow in panel (A)

the presence of voids below the biofilm surface and were processed to obtain DEMs of the biofilm surface topology (Depetris et al., 2019). After 15 days, biofilms developed into a clearly patterned landscape that followed the hydraulic gradient. Tall (up to 1.5 mm) clusters separated by troughs often containing small colonies (<100 μm in height) dominated the biofilm landscape exposed to low flow velocity and shear (Figures 1D and 1F). Biofilms growing under high flow velocity and shear stress developed into thin and coalescing patches densely carpeting the bottom of the flume (Figures 1E and 1G). The formation of these biofilm structures in complex phototrophic biofilms corroborates predictions from modeling and observed in other experimental systems (e.g., De Beer et al., 1994; Chambless and Stewart, 2007; Picioreanu et al., 1998; Stoodley et al., 2001, 2002). The contrasting morphotypes found at both extremes of the hydraulic gradient are hereafter referred to as SFM (slow-flow morphotype) and FFM (fast-flow morphotype).

To quantify the changes in landscape features of mature biofilms (day 15) along the hydraulic gradient, we derived a suite of structural parameters from the DEMs using a moving window (24 mm edge length) approach (Table S1). While biofilm height gradually decreased with increasing shear stress, its volume, porosity, substrate coverage, and accrual rate exhibited significant breakpoints along the gradient in shear stress (Figure 2; Table S2). Biofilm volume, accrual rate, and substrate coverage presented a significant positive relationship with shear stress above the threshold of ~0.08 Pa but not below. This resulted in a more than 2-fold increase in biofilm accrual rate in FFM as compared to SFM. Shear-induced erosion can determine the height of biofilm structures (Chambless and Stewart, 2007), which would explain the observed gradual decrease in biofilm height with increasing shear stress. Given that biofilms developing under high shear are usually denser than those growing under low shear (Beyenal and Lewandowski, 2002), our results suggest that biomass accrual was more efficient under high shear. This is in line with previous experimental findings (Wang et al., 2014) and could be explained by enhanced mass transfer (e.g., Stoodley et al., 1998).

Above the breakpoint shear stress of ~0.08 Pa, biofilm porosity (*sensu* Picioreanu et al., 1998) and textural correlation, a measurement of biofilm aggregation (Haralick et al., 1973) tended to decrease with increasing shear stress (Figure 2, Table S2). Microorganisms compete, besides nutrients, and substrates, also for space, which can become a limiting resource for growth (Lloyd and Allen, 2015). Therefore, the presence of low coverage areas in SFM is remarkable and indicates the existence of processes limiting the full occupancy of the available space. Increased biofilm porosity and aggregation allowing for advection within biofilm troughs may be advantageous when mass transfer is limited under slow flow (De Beer
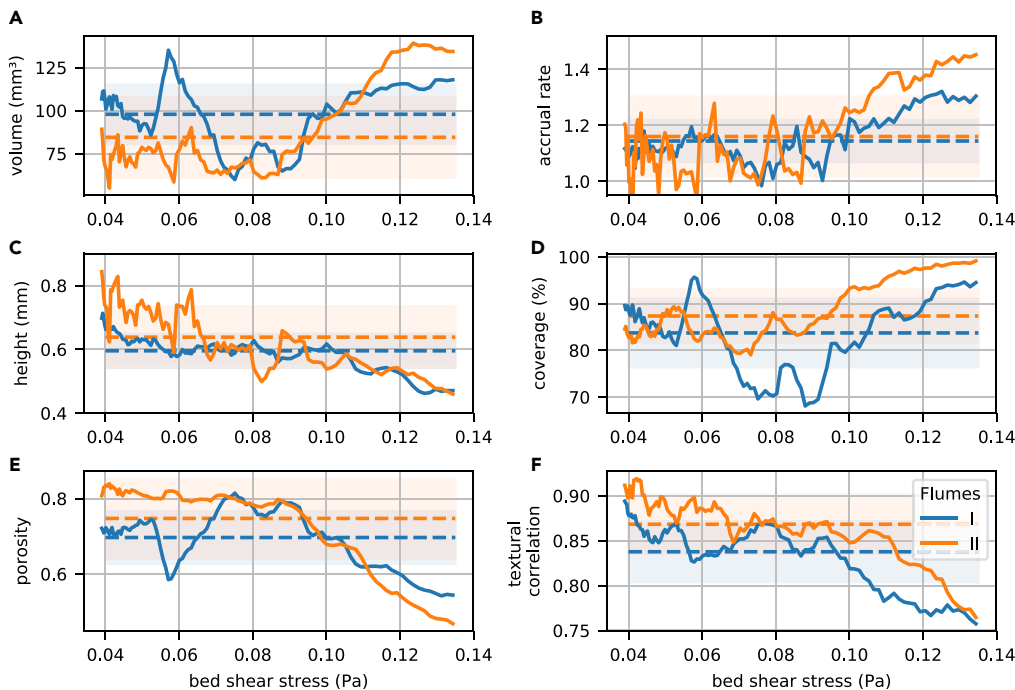
Figure 2. Key properties of phototrophic biofilms change along the hydraulic gradient

Largescale OCT-derived DEMs were used to calculate moving window estimates (solid lines) of biofilm volume (A), accrual rate (B), height (or thickness) (C), coverage (D), porosity (E), and textural correlation (F) along the bed shear stress gradient (day 15; accrual rate was calculated between day 12 and day 15). Dashed lines and shaded areas depict overall averages and standard deviation, respectively. Gray bars indicate, when significant for both replicates, the range of changes in shear stress identified by breakpoint analysis (Table S2).

et al., 1994; Picioreanu et al., 2000). Hence, the observed morphological pattern could represent an adaptive response to mass transfer limitation. Alternatively, clusters separated by voids could form as a consequence of detachment induced by nutrient limitation at the biofilm base combined with erosion of the cells on the biofilm surface (Chambless and Stewart, 2007). However, as noted by Stoodley et al. (2002), architectural differences may also underly differences in the community or EPS composition of the biofilm. Overall, these results suggest that the interplay between fluid flow and both biofilm architecture and growth dynamics are characterized by threshold effects as evoked by previous studies (Hondzo and Wang, 2002; Park et al., 2011; Simões et al., 2007; Wang et al., 2014), and further advocate contrasting mechanisms underlying biofilm morphogenesis.

Limited community turnover between the SFM and the FFM

To test the hypothesis that contrasting morphotypes emerged from differences in community compositions, we sequenced amplicons of the 18S and 16S rRNA genes from the SFM and FFM (day 15) to identify eukaryotic and prokaryotic community members, respectively (Figure S3). Analysis of similarity (Anosim) based on Bray-Curtis similarities, showed no significant differences in community composition (16S rRNA: $R = -0.15$, $p = 0.69$; 18S rRNA: $R = 0.11$, $p = 0.39$) between the two morphotypes. The phototrophic community subset was dominated by Chlorophyceae, classified as *Scenedesmus* sp., contributing 36.6% to the reads in the 18S rRNA amplicon library, followed by *Mougeotia* sp. (Charophyta, 2.4%) and *Achanthidium* sp. (Diatomea, 2.3%). The bacterial communities were dominated by *Luteolibacter sp.* (Verrucomicrobiae, 4.7%), *Flavobacterium sp.* (Bacteroidetes, 2.7%) and not-further classified Sphingomonadaceae (Alpha-Proteobacteria, 2.5%) and Rhodobacteraceae (Alpha-Proteobacteria, 2.5%). *Scenedesmus* sp. is a small (~10 μm in diameter) coenobial and biofilm-forming microalgae that form structurally homogeneous biofilms under laminar flow (Zippel et al., 2007). However, in microbial communities developing under complex hydrodynamic conditions, microalgae may contribute to the formation of complex biofilm architectures (Lawrence and Neu 2003). Given its abundance, it is intuitive to assume that *Scenedesmus* sp. contributed to the here observed biofilm morphogenesis. Strikingly however, the same microalgal and bacterial
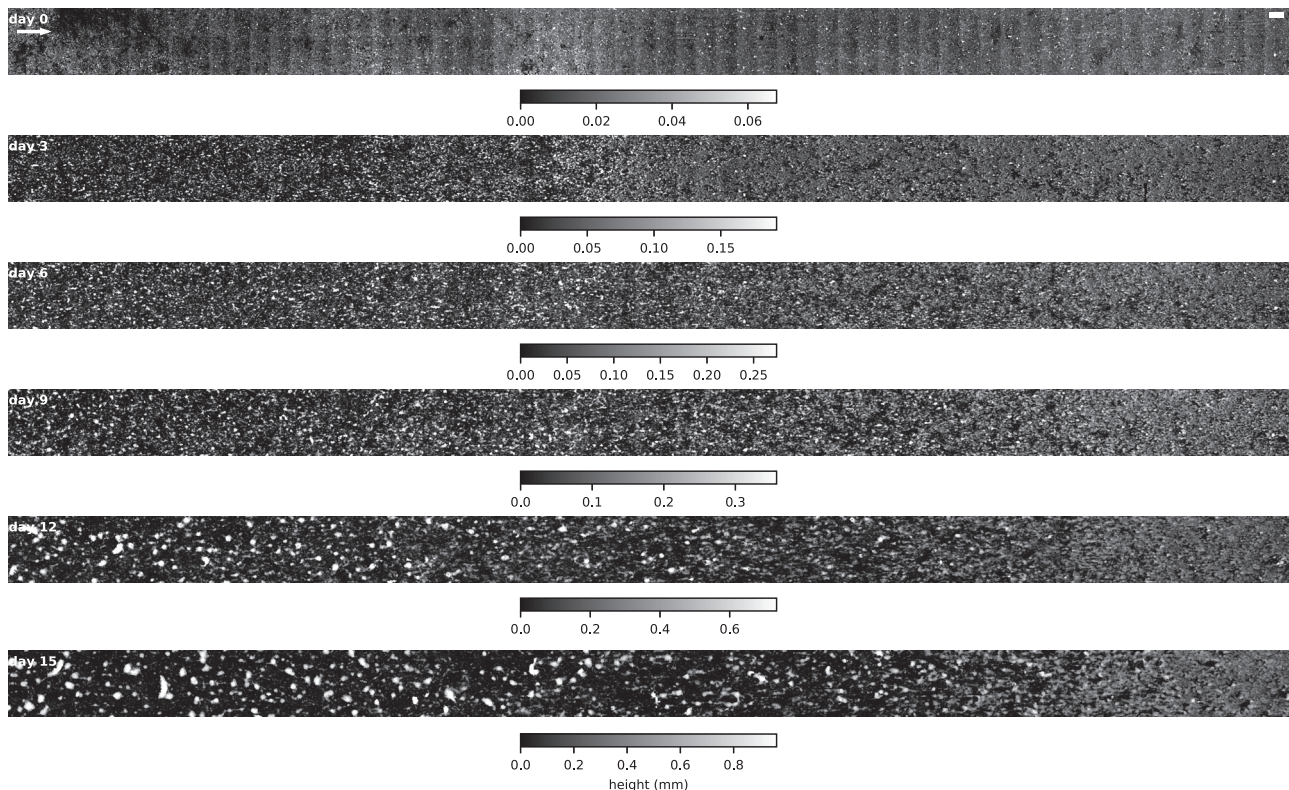
Figure 3. Biofilm morphogenesis over the course of the experiment
The time series of biofilm morphogenesis for the entire hydraulic gradient in flume II is displayed. Note the differences in scales. The arrow indicates flow direction. Scale-bars: 5 mm.

communities were found in both SFM and FFM, reflecting their ability to form differing biofilm morphologies. Our findings evoke architectural plasticity, rather than contrasting community composition, as the process underlying morphological differentiation in the phototrophic biofilms here under study. Architectural plasticity is understood as the remodeling of the biofilms 3-dimensional structure as an adaptive response to their environment (Bridier et al., 2017). It involves, for instance, ecological interactions, the generation of physiological heterogeneities and the differential expression of the extracellular matrix components (Scheidweiler et al., 2019).

Morphogenesis of the SFM and FFM

DEMs of the biofilm surface topology acquired at 3-day intervals (Figure 3) allowed us to address biofilm morphogenesis dynamics. Volume accumulation curves did not differ between SFM and FFM but accrual rates steadily increased over time in the FFM and reached higher values than in the SFM (Figure 4A). Terminal accrual rates (day 12 to day 15) reached 9 mm^3 day^{-1} and 14 mm^3 day^{-1} in the FFM and 3 mm^3 day^{-1} and 5 mm^3 day^{-1} in the SFM (see also Table S1). The analysis of textural correlation showed that aggregation increased steeply at early time-points in the SFM, in contrast to the FFM, while biofilm maximum thickness was consistently higher in the SFM than the FFM at every time point (Figure 4A). Hence, the divergence into morphotypes started early during biofilm growth (day 3) and the SFM, despite being consistently thicker than the FFM, had lower accrual rates in later time-points. In agreement with previous reports (e.g., Hondzo and Wang, 2002; Park et al., 2011), elevated flow velocities, in the range tested here, had a net positive effect on growth, outweighing the effect of shear-induced erosion and scouring.

The presence of protruding biofilm clusters separated by empty areas can have important consequences for the local flow behavior, and related mass transport and drag force (De Beer et al., 1994; Picioreanu et al., 2000; Sudarsan et al., 2016). We compared the areal coverage of protruding clusters (i.e., DEM areas at least two times larger than the local average) and the troughs (i.e., DEM areas at least two times
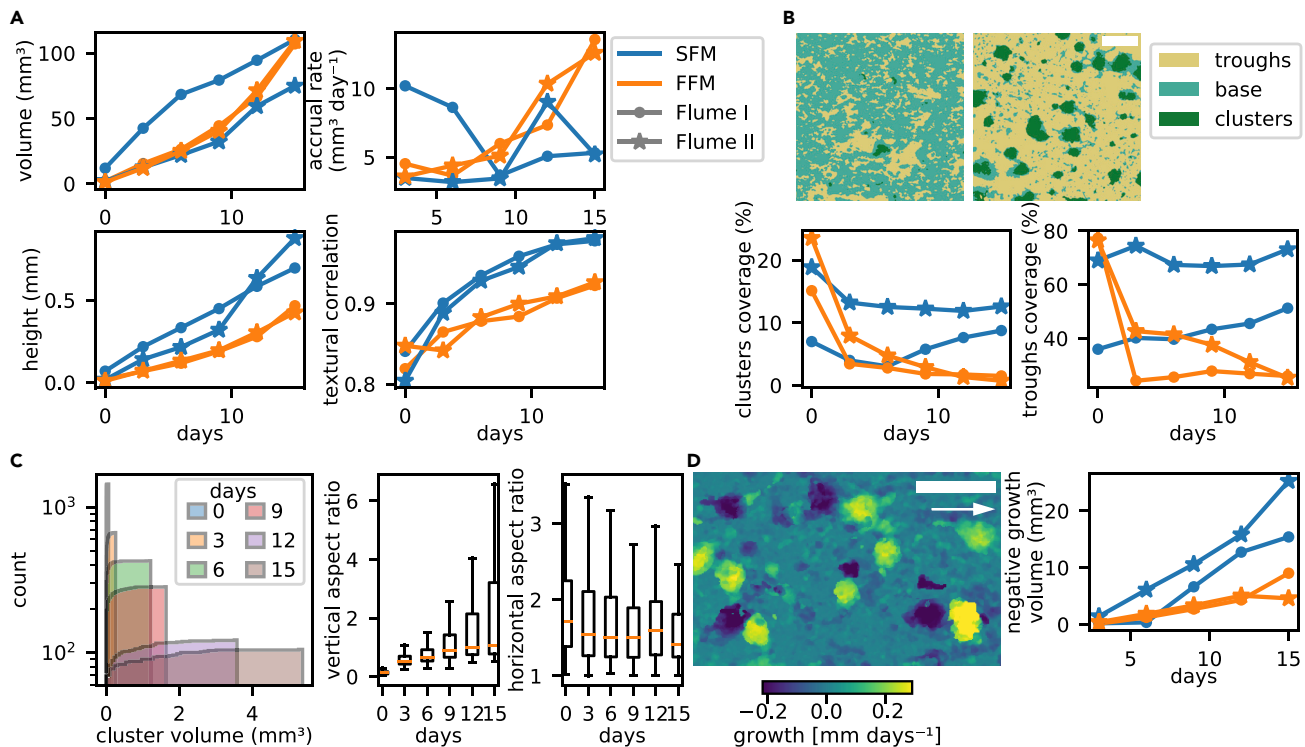
Figure 4. Biofilm morphogenesis differed across hydraulic conditions

The temporal dynamics in biofilm volume, accrual rate, height and aggregation (textural correlation) for the SFM and FFM are shown in panel (A). A segmentation algorithm based on the difference from the local average thickness separated biofilm landscapes into base biofilm, protruding clusters and troughs (B). Shown are the temporal trends in the areal contribution of clusters and troughs. Cumulative histograms demonstrate the simultaneous increase in size and decrease in abundance of SFM clusters, while vertical and horizontal aspect ratios reveal their progressive elongation (C). Subtraction of subsequent DEMs (D, Figure S4) can be interpreted as a spatially explicit estimate of biofilm height variation. Areas with "negative growth" illustrated SFM clusters being detached from the substrate or displaced in flow direction (D). Total biofilm volume affected by "negative growth" increased over time and was higher in the SFM than in the FFM (D). The arrow indicates flow direction. Scale-bars: 5 mm.

lower than the local average) between morphotypes (Figure 4B). The SFM was dominated by troughs (up to 73%) and clusters (up to 11%), whereas the FFM was largely devoid of such cluster-trough sequences and characterized by a base biofilm (up to 74%). The SFM clusters increased in volume (up to 4 mm³) but decreased in abundance over 15 days. They also exhibited an increasingly elongated aspect in the vertical direction and a slight elongation in the flow direction (Figure 4C). As mentioned above, cluster-trough sequences can enhance the external mass transfer toward the biofilm base (De Beer et al., 1994). At the same time, exposed clusters are more susceptible to the drag forces (Dunsmore et al., 2002; Sudarsan et al., 2016).

Despite the limited temporal resolution of the acquired OCT time-series, we observed that the biofilm structures that were dynamic over time. The dynamic rearrangement of the biofilm structures was particularly evident from the subtraction of subsequent DEMs (Figures 4D and S4), in which the local biovolume accumulation and displacement appear as positive and negative pixel gray-level values, respectively. At later time points, entire SFM clusters occasionally sloughed off, while others were apparently pushed in the flow direction. Overall, the FFM appeared more stable in time despite the higher shear stress. Roughly around the shear stress breakpoint, we observed the formation of structures reminiscent of migratory ripples (Figure S4; see also Stoodley et al., 1999). In the SFM, we found that up to 25 mm³ of biovolume was displaced between day 12 and 15, accounting for 33% of the total biovolume (Figure 4D). Hence, although we cannot rigorously quantify biomass detachment and displacement, these qualitative observations support the notion that taller biofilm structures are more exposed to drag force than more homogeneous and self-sheltering structures (e.g., Sudarsan et al., 2016; Dunsmore et al., 2002; Stoodley et al., 2002).

Fluid flow within the SFM troughs provides solutes to the base of the biofilm

In order to assay the effects of surface topography on the local flow patterns, we used 3D numerical simulations to visualize the flow field around two idealized biofilm clusters with a width:height ratio similar to the SFM clusters. The simulated flow field revealed liquid flow into and within troughs between neighboring clusters and showed that fluid is advected into troughs predominantly via the vertical (u_z) and the lateral (u_y) components of velocity (Figure 5A). The simulated velocity field around two idealized biofilm clusters displayed downward and lateral fluid motions within the trough region between the clusters. Streamlines originating from upstream of the clusters entered the trough with velocities up to 10% of the mean flow velocity. Simulations further indicated that a fluid element entering the trough from the top recirculated in the trough region and reached the center of the region in approximately 1.5 min. Furthermore, we noted the formation of a vortex ring that could lead to enhanced fluid mixing in the trough region (Figure 5A). In line with previous models (Picioreanu et al., 2000), these simulations suggest that advection within troughs is relevant for solute transport and replenishment, which may be further facilitated by the formation of vortices.

Motivated by these simulations, we tested for the advective replenishment of oxygen within the biofilm troughs by measuring oxygen microprofiles across and around biofilm clusters (in darkness). Microbial respiration is expected to reduce oxygen concentrations in stagnant zones where diffusion is the sole source of oxygen replenishment (De Beer et al., 1994). However, we found that dissolved oxygen concentration did not differ between the troughs and the bulk fluid (Figure 5B), supporting the notion of oxygen replenishment by multi-directional advective transport. We did not detect a diffusive boundary layer around the biofilm structures in both the SFM and the FFM (sensitivity ~50 μm; Figures 5B and S5). These results agree with other empirical observations and modeling predictions from earlier studies on heterogeneous biofilms (De Beer et al., 1994; Picioreanu et al., 2000; Stoodley et al., 1997). However, the observation that the diffusive boundary layer around SFM clusters and troughs must be thin (<50 μm) eliminates external mass transfer resistance as a driver of the formation of a rough, finger-like architecture (Picioreanu et al., 1998). In contrast, both the measured oxygen microprofiles and fluid dynamic simulation suggest that the transport of solutes from the troughs toward the clusters may sustain microbial activity and growth at the biofilm base.

Oxygen concentration profiles within biofilm architectures reveal chemical micro-niches

Chemical gradients figure among the emergent properties in biofilms that result from internal mass transfer resistance and potentially drive the small-scale diversification of biological processes with large-scale consequences (Flemming and Wingender, 2010; Stewart and Franklin, 2008). For instance, limited mass transport within densely packed cells and their extracellular matrix can lead to nutrients deprivation in the deeper biofilm layers, potentially triggering sloughing (Chambless and Stewart, 2007; Hunt et al., 2004; Xavier et al., 2005). To map the spatial distribution of oxygen inside the biofilm, we measured multiple oxygen profiles within the SFM (n = 35) and FFM (n = 27) structures (few representative profiles are reported in Figure 6A). Oxygen concentrations (in light, dark, and the difference between light and dark) were more widely distributed in the SFM than in the FFM (robust Brown-Forsythe Levene-type test, p value < 0.01) (Figures 6B and Table S3). This corroborates the notion that structural heterogeneity, which is higher in SFM than FFM, leads to a heterogeneous distribution of chemical micro-niches in phototrophic biofilms.

Under dark conditions, dissolved oxygen reached a lower concentration in the SFM (40 μmol L^{-1}) than in the FFM (178 μmol L^{-1}), while the opposite was the case under light (SFM: 353 μmol L^{-1}; FFM: 260 μmol L^{-1}). Also, when comparing measurements at the same biofilm depths, oxygen concentrations reached more extreme values in the SFM compared to the FFM (t-tests, p *values* < 0.01 for both light conditions and depths into the biofilm from 0.05 mm to 0.25 mm) (Figure 6C and Table S4). These patterns are unlikely driven by differences in oxygen diffusivity, as biofilms grown under high shear are usually denser and less permeable to oxygen than their low-shear counterparts (Beyenal and Lewandowski, 2002). Hence, the gentler oxygen gradients within the FFM could be driven either by lower metabolic rates or advective oxygen transport inside the biofilm, but these processes cannot be disentangled in our experimental setup.

Next, we mapped oxygen concentrations across individual SFM clusters in dark conditions (Figure S6). We found that oxygen within SFM clusters was less depleted close to the cluster side walls compared to their inner cores (t-tests, p *values* < 0.01 for depths ranging from 0.1 mm to 0.5 mm) (Figure 6D and Table S5). This observation supports the notion that advective transport within troughs replenishes oxygen through
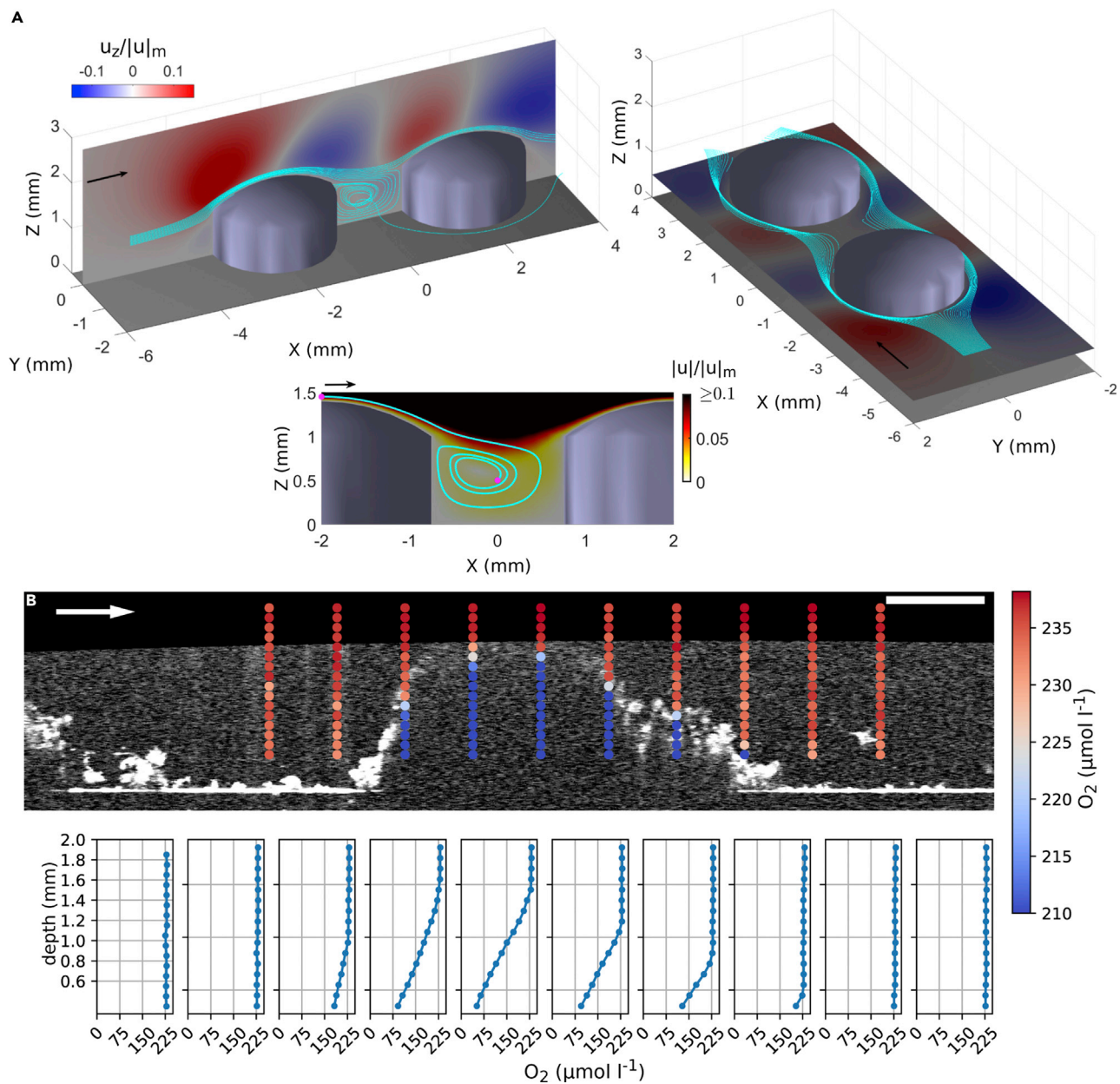
Figure 5. Numerical simulations and measured oxygen microprofiles suggest the presence of fluid flow around biofilm clusters

Shown are the outcome of three-dimensional numerical simulations around two idealized biofilm clusters.

(A) Provides the normalized vertical velocity and the lateral velocity components in the vertical symmetry plane (y = 0 mm) and a horizontal plane (z = 0.5 mm) superposed with selected streamlines. The lower subpanel shows the normalized velocity magnitude in the symmetry plane superposed with a streamline that demonstrates the fluid motion in the trough.

(B) Shows representative oxygen measurements within and around a biofilm cluster (SFM) superimposed onto the respective OCT scan. Panel B illustrates oxygen microprofiles measured around and within biofilm clusters. Each point depicts the concentration of a single oxygen concentration measurement. Corresponding oxygen microprofiles are shown below. The arrow indicates the flow direction. Scale bar: 5 mm.

SFM cluster walls. However, compared to the FFM, this effect only insufficiently supplies oxygen to the cores of SFM clusters, which were, compared to the FFM, more oxygen depleted in dark conditions (and more saturated when exposed to light). Given the low half-saturation coefficient for dissolved oxygen for bacteria (Hao et al., 1983), it is unlikely that oxygen itself limited the metabolic activity of the biofilms under study. However, it is conceivable that other solutes, such as nutrients and metabolic waste products,
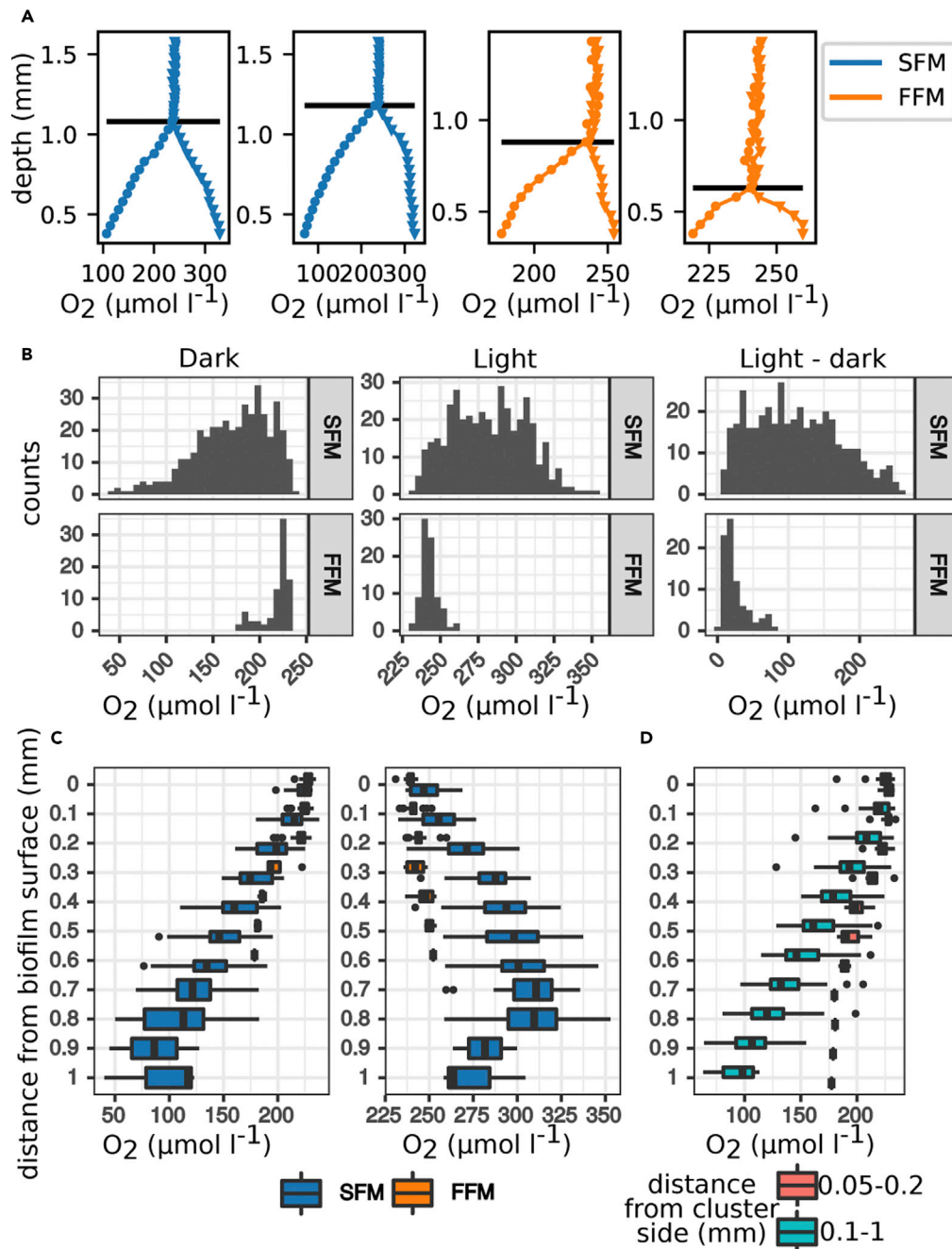
Figure 6. Oxygen microprofiling suggests a more heterogeneous distribution of chemical micro-niches in the SFM compared to the FFM

Reported are representative oxygen microprofiles measured within SFM and FFM in light (triangles) and dark (circles) (A). Horizontal lines indicate the estimated position of the biofilm surface. Oxygen concentration and the difference in oxygen concentration between light and dark conditions were more heterogeneously distributed in the SFM than in the FFM (B). The distribution of oxygen concentration measured at the same biofilm depth (pooled in 100 μm steps) are compared between morphotypes (C) and at different distances from the SFM clusters walls (D, dark conditions).

will follow similar spatial dynamics and potentially induce stress responses in the cores and at the base of the SFM. Therefore, differential detachment induced by nutrients limitation remains a potential mechanism that could underly the formation of clusters separated by voids under low shear.

We did not attempt to infer metabolic rates from the oxygen profiles because these could be compromised by advective transport within the biofilm matrix. However, we calculated the ratio between the oxygen gradients (from 0.05 to 0.15 mm depth) in light and dark as a proxy for net autotrophic *versus* heterotrophic aerial oxygen fluxes. Light:dark ratios averaged around 1 and were not significantly different between the SFM and the FFM (Welch's test, p *value* = 0.23, Figure S7), which indicates a balance between net oxygen production and consumption in both morphotypes.

Conclusions

Combining 3D imaging with sequencing, numerical simulations of fluid flow, and oxygen microprofiling, we described architectural patterns in a complex phototrophic biofilm growing under a quasi-natural flow conditions. Over a relatively short hydraulic gradient, we observed strikingly diverging biofilm architectures despite limited community turnover. Clusters separated by troughs developed under low shear stress, while a more homogeneous biofilm layer covered the substrate under high-shear. Streams are characterized by a remarkable heterogeneity in hydraulic conditions, both on short- and large-spatial range. Our results indicate that the architecture of benthic biofilms may plastically respond to the hydraulic conditions in their habitat, even in the absence of strong shifts in the community composition.

Several experimental and modeling studies have previously investigated biofilms architectures under controlled laboratory conditions, providing numerous mechanistic hypotheses regarding their emergence. On one side, biofilm morphologies analogous to those observed here have been described across biofilm communities and spatial scales, and hence seem to be rather universal. On the other, our results confirm that the advective replenishment of oxygen within the biofilm troughs as well as the dynamic displacement and detachment of isolated clusters, may influence the morphogenesis of complex phototrophic biofilms in their natural environment. Our observations seem to exclude external mass transfer limitation as a driver of biofilm morphogenesis under the studied hydraulic conditions, whereas a combination of differential detachment induced by nutrients limitation and erosion of cells from the biofilm surface remains a viable explanation. We further observed an abrupt morphological transition around a threshold shear stress of ~0.08 Pa. Mechanical properties of the different architectures may lead to this threshold effect, however this remains to be addressed in future theoretical and empirical studies. Overall, our findings suggest that a tight coupling between architectural plasticity, chemical heterogeneity and mechanical resistance to shear affects the formation of the meso-scale patterns observed in biofilms that coat the benthic zones in streams and rivers.

Limitations of the study

Following an approach often used in landscape ecology (Calders et al., 2020), we inferred the functional links between hydraulic conditions and biofilm morphogenesis from their spatial correlation. While this approach allowed us to study complex phototrophic communities at high resolution and under realistic hydraulic conditions, we cannot account for all potential effects. For instance, biomass may accumulate downstream, potentially oozing in the direction of the flow. This possibility seems unlikely, as shear and turbulence in the flume fast-flow region were strong enough to detach biomass that was just loosely adherent to the substrate, and did not permit the sedimentation of aggregates from the water column (visual observation). Furthermore, we started detecting a morphological shift between contrasting hydraulic conditions at early stages in biofilm development (3 days), when the accumulated biovolume was still remarkably low and no significant displacement of the biomass occurred yet. Nonetheless, the relationship between biofilm architecture and hydraulic conditions remains correlational and further experiments would be required to rigorously test any causal link. Working with complex communities and natural surface water as growth medium allows the formation of diverse biofilms relevant for stream ecosystems, but seasonal variation in inflow medium and seed community reduced the repeatability of the experiments. However, the communities that we sampled and the patterns that we observed are realistic and informative. The raw lake water used was filtered (nominal pore size 50 μm), but this removed just larger grazers and did not completely eliminate grazing pressure, which could have further modulated the morphology of the studied biofilms (Böhme et al., 2009; Weitere et al., 2018). The flumes were constructed from plexiglass and this smooth substrate may have affected the observed dynamics to some extent. Nonetheless, the two biofilm morphotypes exhibited structural differences leading to diverging structural resistance, which are likely independent on the type of substrate colonized. OCT has a limited penetration depth within biofilms and imaging depth in water; as a consequence, structures taller than ~1.2 mm were not reliably

imaged, which may have caused an underestimation of the total volume, accrual rate and biofilm thickness, particularly at later time-points and under slow flow.

Resource availability

Lead contact

Further information and requests for resources should be directed to and will be fulfilled by the Lead Contact, Tom Battin (tom.battin@epfl.ch).

Materials availability

This study did not generate new unique reagents.

Data and code availability

Raw OCT scans, processed DEMs, and oxygen microprofile data have been deposited at https://figshare. com/projects/Data_for_Morphogenesis_of_phototrophic_biofilms_is_controlled_by_hydraulic_constraints_ and_enabled_by_architectural_plasticity/87296. Raw sequences are available at the European Nucleotide Archive (ENA) under accession number PRJEB39886. Code used for image acquisition, processing and analysis is available under https://figshare.com/projects/Data_for_Morphogenesis_of_phototrophic_ biofilms_is_controlled_by_hydraulic_constraints_and_enabled_by_architectural_plasticity/87296.

METHODS

All methods can be found in the accompanying Transparent Methods supplemental file.

SUPPLEMENTAL INFORMATION

Supplemental information can be found online at https://doi.org/10.1016/j.isci.2021.102067.

AUTHOR CONTRIBUTIONS

AD, TJB, and HP designed the experiments; AD conducted the experiment and analyzed the data; MK advised on microsensor measurements and data analyses; PDA and AB performed the computational simulations of fluid dynamics around idealized biofilms clusters; HB and AN performed the computational simulations of fluid dynamics within the flumes; AD wrote the paper with support from all other authors.

DECLARATION OF INTERESTS

The authors declare no competing interests.

REFERENCES

Battin, T.J., Kaplan, L.A., Newbold, J.D., Cheng, X., and Hansen, C. (2003). Effects of current velocity on the Nascent architecture of stream microbial biofilms. Appl. Environ. Microbiol. 69, 5443–5452.

Battin, T.J., Sloan, W.T., Kjelleberg, S., Daims, H., Head, I.M., Curtis, T.P., and Eberl, L. (2007). Microbial landscapes: new paths to biofilm research. Nat. Rev. Microbiol. 5, 76–81.

Battin, T.J., Besemer, K., Bengtsson, M.M., Romani, A.M., and Packmann, A.I. (2016). The ecology and biogeochemistry of stream biofilms. Nat. Rev. Microbiol. 14, 251–263.

De Beer, D., Stoodley, P., Roe, F., and Lewandowski, Z. (1994). Effects of biofilm structures on oxygen distribution and mass transport. Biotechnol. Bioeng. 43, 1131–1138.

De Beer, D., Stoodley, P., and Lewandowski, Z. (1996). Liquid flow and mass transport in heterogeneous biofilms. Water Res. 30, 2761–2765.

Beyenal, H., and Lewandowski, Z. (2002). Internal and external mass transfer in biofilms grown at various flow velocities. Biotechnol. Prog. 18, 55–61.

Bjarnsholt, T., Alhede, M., Alhede, M., Eickhardt-Sørensen, S.R., Moser, C., Kühl, M., Jensen, P.Ø., and Høiby, N. (2013). The in vivo biofilm. Trends Microbiol. 21, 466–474.

Böhme, A., Risse-Buhl, U., and Küsel, K. (2009). Protists with different feeding modes change biofilm morphology. FEMS Microbiol. Ecol. 69, 158–169.

Bridier, A., Piard, J.-C., Pandin, C., Labarthe, S., Dubois-Brissonnet, F., and Briandet, R. (2017). Spatial organization plasticity as an adaptive driver of surface microbial communities. Front. Microbiol. 8, 1364.

Calders, K., Phinn, S., Ferrari, R., Leon, J., Armston, J., Asner, G.P., and Disney, M. (2020). 3D imaging insights into forests and coral Reefs. Trends Ecol. Evol. 35, 6–9.

Chambless, J.D., and Stewart, P.S. (2007). A three-dimensional computer model analysis of three hypothetical biofilm detachment mechanisms. Biotechnol. Bioeng. 97, 1573–1584.

Cremer, J., Segota, I., Yang, C., Arnoldini, M., Sauls, J.T., Zhang, Z., Gutierrez, E., Groisman, A., and Hwa, T. (2016). Effect of flow and peristaltic mixing on bacterial growth in a gut-like channel. Proc. Natl. Acad. Sci. U S A 113, 11414–11419.

Depetris, A., Wiedmer, A., Wagner, M., Schäfer, S., Battin, T.J., and Peter, H. (2019). Automated 3D optical coherence tomography to elucidate biofilm morphogenesis over large spatial scales. J. Vis. Exp. https://doi.org/10.3791/59356.

Dietrich, L.E.P., Okegbe, C., Price-Whelan, A., Sakhtah, H., Hunter, R.C., and Newman, D.K. (2013). Bacterial community morphogenesis is intimately linked to the intracellular redox state. J. Bacteriol. 195, 1371–1380.

Drescher, K., Dunkel, J., Nadell, C.D., van Teeffelen, S., Grnja, I., Wingreen, N.S., Stone, H.A., and Bassler, B.L. (2016). Architectural transitions in Vibrio cholerae biofilms at single-cell resolution. Proc. Natl. Acad. Sci. U S A 113, E2066–E2072.

Dunsmore, B.C., Jacobsen, A., Hall-Stoodley, L., Bass, C.J., Lappin-Scott, H.M., and Stoodley, P. (2002). The influence of fluid shear on the structure and material properties of sulphate-reducing bacterial biofilms. J. Ind. Microbiol. Biotechnol. 29, 347–353.

Dzubakova, K., Peter, H., Bertuzzo, E., Juez, C., Franca, M.J., Rinaldo, A., and Battin, T.J. (2018). Environmental heterogeneity promotes spatial resilience of phototrophic biofilms in streambeds. Biol. Lett. 14, 20180432.

Findlay, R.H., and Battin, T.J. (2016). The microbial ecology of benthic environments. In Manual of Environmental Microbiology, M.V. Yates, C.H. Nakatsu, R.V. Miller, and S.D. Pillai, eds. (American Society for Microbiology), pp. 1–20, https://doi.org/10.1128/9781555818821.ch4.2.1.

Flemming, H.-C., and Wingender, J. (2010). The biofilm matrix. Nat. Rev. Microbiol. 8, 623–633.

Flemming, H.-C., and Wuertz, S. (2019). Bacteria and archaea on Earth and their abundance in biofilms. Nat. Rev. Microbiol. 17, 247–260.

Flemming, H.-C., Wingender, J., Szewzyk, U., Steinberg, P., Rice, S.A., and Kjelleberg, S. (2016). Biofilms: an emergent form of bacterial life. Nat. Rev. Microbiol. 14, 563–575.

Guilbaud, M., Piveteau, P., Desvaux, M., Brisse, S., and Briandet, R. (2015). Exploring the diversity of Listeria monocytogenes biofilm architecture by high-throughput confocal laser scanning microscopy and the predominance of the honeycomb-like morphotype. Appl. Environ. Microbiol. 81, 1813–1819.

Hall-Stoodley, L., Costerton, J.W., and Stoodley, P. (2004). Bacterial biofilms: from the natural environment to infectious diseases. Nat. Rev. Microbiol. 2, 95–108.

Hao, O.J., Richard, M.G., Jenkins, D., and Blanch, H.W. (1983). The half-saturation coefficient for dissolved oxygen: a dynamic method for its determination and its effect on dual species competition. Biotechnol. Bioeng. 25, 403–416.

Haralick, R.M., Shanmugam, K., and Dinstein, I. (1973). Textural features for image classification. IEEE Trans. Syst. Man. Cybern. Smc-3, 610–621.

Hondzo, M., and Wang, H. (2002). Effects of turbulence on growth and metabolism of periphyton in a laboratory flume. Water Resour. Res. 38, 13-1–13-19.

Hunt, S.M., Werner, E.M., Huang, B., Hamilton, M.A., and Stewart, P.S. (2004). Hypothesis for the role of nutrient starvation in biofilm detachment. Appl. Environ. Microbiol. 70, 7418–7425.

Lawrence, J.R., and Neu, T.R. (2003). Microscale analyses of the formation and nature of microbial biofilm communities in river systems. Rev. Environ. Sci. Biotech. 2, 85–97.

Lloyd, D.P., and Allen, R.J. (2015). Competition for space during bacterial colonization of a surface. J. R. Soc. Interface 12, 20150608.

Van Loosdrecht, M.C.M., Heijnen, J.J., Eberl, H., Kreft, J., and Picioreanu, C. (2002). Mathematical modelling of biofilm structures. Antonie van Leeuwenhoek. Int. J. Gen. Mol. Microbiol. 81, 245–256.

Milferstedt, K., Pons, M.-N., and Morgenroth, E. (2009). Analyzing characteristic length scales in biofilm structures. Biotechnol. Bioeng. 102, 368–379.

Neu, T.R., and Lawrence, J.R. (2006). Development and structure of microbial biofilms in river water studied by confocal laser scanning microscopy. FEMS Microbiol. Ecol. 24, 11–25.

Park, A., Jeong, H.-H., Lee, J., Kim, K.P., and Lee, C.-S. (2011). Effect of shear stress on the formation of bacterial biofilm in a microfluidic channel. Biochip J. 5, 236–241.

Picioreanu, C., van Loosdrecht, M.C.M., and Heijnen, J.J. (1998). Mathematical modeling of biofilm structure with a hybrid differential-discrete cellular automaton approach. Biotechnol. Bioeng. 58, 101–116.

Picioreanu, C., van Loosdrecht, M.C.M., and Heijnen, J.J. (2000). A theoretical study on the effect of surface roughness on mass transport and transformation in biofilms. Biotechnol. Bioeng. 68, 355–369.

Picioreanu, C., Vrouwenvelder, J.S., and van Loosdrecht, M.C.M. (2009). Three-dimensional modeling of biofouling and fluid dynamics in feed spacer channels of membrane devices. J. Memb. Sci. 345, 340–354.

Rietkerk, M. (2004). Self-Organized patchiness and catastrophic shifts in ecosystems. Science 305, 1926–1929.

Rossy, T., Nadell, C.D., and Persat, A. (2019). Cellular advective-diffusion drives the emergence of bacterial surface colonization patterns and heterogeneity. Nat. Commun. 10, 2471.

Scheidweiler, D., Peter, H., Pramateftaki, P., de Anna, P., and Battin, T.J. (2019). Unraveling the biophysical underpinnings to the success of multispecies biofilms in porous environments. ISME J. 13, 1700–1710.

Simões, M., Pereira, M.O., Sillankorva, S., Azeredo, J., and Vieira, M.J. (2007). The effect of hydrodynamic conditions on the phenotype of Pseudomonas fluorescens biofilms. Biofouling 23, 249–258.

Stewart, P.S. (2012). Mini-review: convection around biofilms. Biofouling 28, 187–198.

Stewart, P.S., and Franklin, M.J. (2008). Physiological heterogeneity in biofilms. Nat. Rev. Microbiol. 6, 199–210.

Stoodley, P., Yang, S., Lappin-Scott, H., and Lewandowski, Z. (1997). Relationship between mass transfer coefficient and liquid flow velocity in heterogenous biofilms using microelectrodes and confocal microscopy. Biotechnol. Bioeng. 56, 681–688.

Stoodley, P., Dodds, I., Boyle, J.D., and Lappin-Scott, H.M. (1998). Influence of hydrodynamics and nutrients on biofilm structure. J. Appl. Microbiol. 85, 19S–28S.

Stoodley, P., Lewandowski, Z., Boyle, J.D., and Lappin-Scott, H.M. (1999). The formation of migratory ripples in a mixed species bacterial biofilm growing in turbulent flow. Environ. Microbiol. 1, 447–455.

Stoodley, P., Wilson, S., Hall-Stoodley, L., Boyle, J.D., Lappin-Scott, H.M., and Costerton, J.W. (2001). Growth and detachment of cell clusters from mature mixed-species biofilms. Appl. Environ. Microbiol. 67, 5608–5613.

Stoodley, P., Cargo, R., Rupp, C.J., Wilson, S., and Klapper, I. (2002). Biofilm material properties as related to shear-induced deformation and

detachment phenomena. J. Ind. Microbiol. Biotechnol. *29*, 361–367.

Sudarsan, R., Ghosh, S., Stockie, J.M., and Eberl, H.J. (2016). Simulating biofilm deformation and detachment with the immersed boundary method. Commun. Comput. Phys. *19*, 682–732.

Thar, R., and Kühl, M. (2005). Complex pattern formation of marine gradient bacteria explained by a simple computer model. FEMS Microbiol. Lett. *246*, 75–79.

Wagner, M., Taherzadeh, D., Haisch, C., and Horn, H. (2010). Investigation of the mesoscale structure and volumetric features of biofilms using optical coherence tomography. Biotechnol. Bioeng. *107*, 844–853.

Wang, C., Miao, L., Hou, J., Wang, P., Qian, J., and Dai, S. (2014). The effect of flow velocity on the distribution and composition of extracellular polymeric substances in biofilms and the detachment mechanism of biofilms. Water Sci. Technol. *69*, 825–832.

Wang, L., Keatch, R., Zhao, Q., Wright, J.A., Bryant, C.E., Redmann, A.L., and Terentjev, E.M. (2018). Influence of type I fimbriae and fluid shear stress on bacterial behavior and multicellular architecture of early Escherichia coli biofilms at single-cell resolution. Appl. Environ. Microbiol. *84*, 1–13.

Weitere, M., Erken, M., Majdi, N., Arndt, H., Norf, H., Reinshagen, M., Traunspurger, W., Walterscheid, A., and Wey, J.K. (2018). The food web perspective on aquatic biofilms. Ecol. Monogr. *88*, 543–559.

Xavier, J.B., Picioreanu, C., and Van Loosdrecht, M.C.M. (2005). A framework for multidimensional modelling of activity and structure of multispecies biofilms *7*, 1085–1103.

Xavier, J.B., Martinez-Garcia, E., and Foster, K.R. (2009). Social evolution of spatial patterns in bacterial biofilms: when conflict drives disorder. Am. Nat. *174*, 1–12.

Yan, J., Fei, C., Mao, S., Moreau, A., Wingreen, N.S., Košmrlj, A., Stone, H.A., and Bassler, B.L. (2019). Mechanical instability and interfacial energy drive biofilm morphogenesis. Elife *8*, 1–28.

Zippel, B., Rijstenbil, J., and Neu, T.R. (2007). A flow-lane incubator for studying freshwater and marine phototrophic biofilms. J. Microbiol. Methods. *70*, 336–345.

Supplemental Information

Morphogenesis and oxygen dynamics

in phototrophic biofilms growing

across a gradient of hydraulic conditions

Anna Depetris, Hannes Peter, Ankur Deep Bordoloi, Hippolyte Bernard, Amin Niayifar, Michael Kühl, Pietro de Anna, and Tom Jan Battin

Supplemental Tables

Table S1. Morphological features of SFM and FFM at the two extremes of the flow velocity gradient after 15 days of growth, Related to Figure 1. The reported accrual rates refer to the time interval between day 12 and day 15.

| | flume | hydraulic conditions | | morphological features | | | | | |
		flow velocity [m s^{-1}]	shear stress [Pa]	volume [mm^3]	accrual rate [mm^3 day^{-1}]	height [mm]	coverage [%]	porosity	textural correlation
SFM	I	0.059	0.04	107	3.73	0.7	90	0.72	0.89
	II	0.059	0.04	89	5.04	0.84	85	0.81	0.91
FFM	I	0.135	0.13	118	9.18	0.47	95	0.54	0.76
	II	0.135	0.13	134	13.96	0.46	99	0.47	0.76

Table S2. Segmented-regression analysis of the morphological gradient, Related to Figure 2.
We tested for the presence of a breakpoint, separating two regions of the morphological gradient with contrasting relationship with shear stress, using the Davies' test for a non-zero difference-in-slope parameter of the segmented regression. The bed-shear stress breakpoint, standard error (SE) estimates and p-vlaues are reported as well as the adjusted R^2 of the segmented regression. When the Davies' test was not significant, the adjusted R^2 of a linear model is reported. The statistical significance of trends below and above the breakpoint shear stress (low and high shear respectively), was tested with the modified version of the Mann-Kendall test for autocorrelated series. Significant trends were evaluated with a linear model, whose slope are reported (units of the variable $* \text{Pa}^{-1}$). When no significant breakpoint was observed, the Mann-Kendall test was performed on the entire data set.

| | | Davies' test | | | | Mann-Kendall test | | | | linear model |
| | | | | | | SFM | | FFM | | |
	flume	breakpoint shear [Pa]	SE	p-value	adj. R^2	corrected Z	p-value	corrected Z	p-value	slope
volume [mm³]	I	0.085	0.003	<0.05	0.50	-1.85	0.06	2.63	<0.01	1108
	II	0.084	0.002	<0.01	0.92	-0.62	0.53	3	<0.01	1661
accrual rate [mm³ day⁻¹]	I	0.089	0.006	<0.01	0.78	-1.16	0.24	2.63	<0.01	190.5
	II	0.083	0.006	<0.05	0.89	-0.62	0.53	3.00	<0.01	281.9
height [mm]	I	-	-	0.19	0.78	-3.3	<0.01	-	-	-1.69
	II	-	-	0.26	0.76	-4.2	<0.01	-	-	-3.02
coverage [%]	I	0.087	0.002	<0.01	0.67	-2.26	0.02	2.63	<0.01	568
	II	0.073	0.002	<0.01	0.86	-0.72	0.47	3.34	<0.01	314
porosity	I	0.089	0.002	<0.01	0.68	1.44	0.15	-2.63	<0.01	-5.7
	II	0.089	0.001	<0.01	0.99	-2.81	<0.01	-2.63	<0.01	-7.5
textural correlation	I	-	-	0.10	0.75	-2.98	<0.01	-	-	-1.07
	II	0.111	0.002	<0.01	0.92	-12.83	<0.01	-1.04	0.3	-0.76

Table S3. Statistics of the distribution of the dissolved oxygen concentration in the slow- and fast- flow morphotypes (SFM and FFM), Related to Figure 5 and Figure 6. We obtained several profiles of dissolved oxygen concentrations in different locations within the SFM and FFM, under light and dark conditions (flume II). The features of the distribution of oxygen concentrations (points from all profiles were pooled) are reported.

|		FFM	SFM
	number of profiles	27	35
	number of points	84	406
	0.1 quantile	189.9	115.9
	0.9 quantile	230.9	219.2
dark	maximum	235.1	238.1
$[\mu mol\ O_2\ L^{-1}]$	mean	218.1	170.8
	median	224.2	177.1
	minimum	177.9	40.2
	0.1 quantile	237.0	250.9
	0.9 quantile	250.7	313.6
light	maximum	259.8	352.9
$[\mu mol\ O_2\ L^{-1}]$	mean	242.6	282.6
	median	241.8	282.8
	minimum	230.9	232.5

Table S4. Test statistics, Related to Figure 6. T-tests for unpaired samples with uneven variances to test for differences in oxygen concentration at different depth within the biofilm among profiles taken within the SFM and FFM in light and darkness, respectively. Measurements were pooled in 0.1 mm steps.

| depth within biofilm [mm]	dark p-value	light p-value	n_{SFM}	n_{FFM}
0.05	2.7e-02	1.17e-04	24	24
0.05-0.15	1.12e-06	4.40e-11	58	24
0.15-0.25	4.57e-13	6.73e-22	86	23
0.25-0.35	4.74e-02	6.16e-06	32	4
0.35-0.45	2.73e-10	3.19e-06	74	5
0.45-0.55	2.38e-08	2.84e-10	39	3

Table S5. Test statistics, Related to Figure 6. T-test for unpaired samples with uneven variances to test for differences in oxygen concentration at different depths within the biofilm among profiles taken within the SFM clusters in the dark. Measurements were pooled in 0.1 mm steps.

| depth within biofilm [mm]	p-value	n dist[0.05-0.2]	n dist[0.2-1]
0.05	0.22	6	14
0.05-0.15	0.03	9	33
0.15-0.25	0.003	9	33
0.25-0.35	0.004	7	32
0.35-0.45	0.008	6	30
0.45-0.55	0.004	5	29

Supplemental Figures
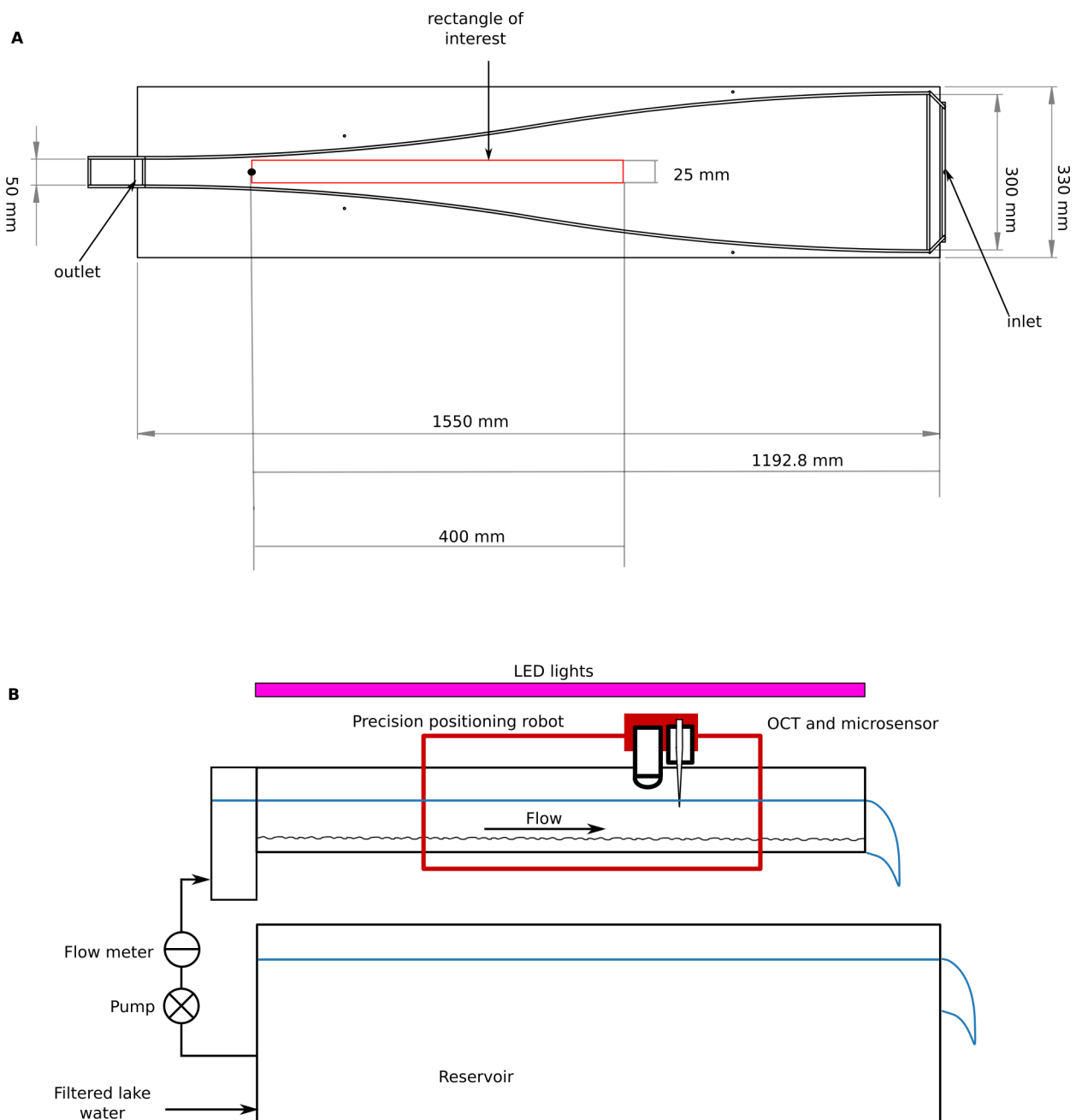
Supplemental Figure S1. Experimental Design, Related to Figure 1. Plexiglass flumes were designed with the represented geometry to obtain a flow velocity gradient, increasing in the direction of the flow. The "rectangle of interest" indicates the position of the biofilm characterized in this study. The flumes had a total depth of 50 mm, while the depth of the water was ~ 22 mm (A). Filtered lake water was continuously pumped into a large reservoir, from which it was pumped into the flume. The flow rate was controlled with a flow meter. The water was fully recirculated into the reservoir. Light was provided with LED lights, while the OCT probe and the microsensor were mounted on a robot that allowed to precisely control their positioning (B).
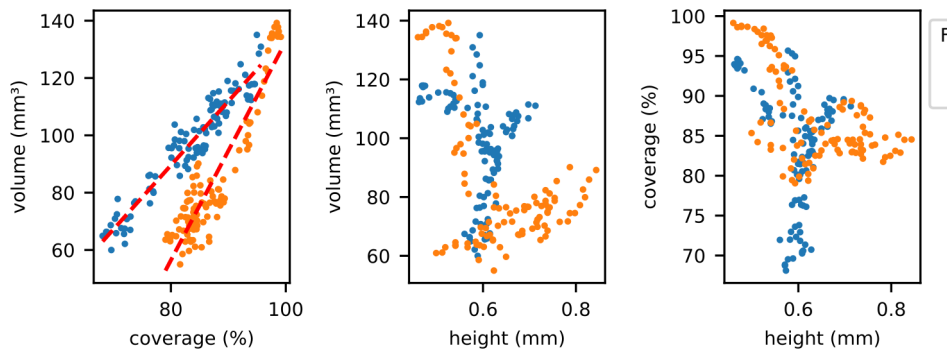
Supplemental Figure S2. Biovolume is correlated to surface coverage rather than to biofilm height, Related to Figure 2. We found a significant positive correlation between the volume accumulated in a square moving window (24 mm edge length) along the hydraulic gradient (flume II is showed in Figure 1 of the main text) and total coverage in the same window (lm, $slope_I = 2.23$; $slope_{II} = 3.82$; $R^2_I = 0.96$, $R^2_{II} = 0.93$; p-value < 0.01 for both). In contrast, maximum height of the biofilm, calculated as the 0.99 percentile of the height distribution, was found to have a negative and non-linear relationship with accumulated volume.
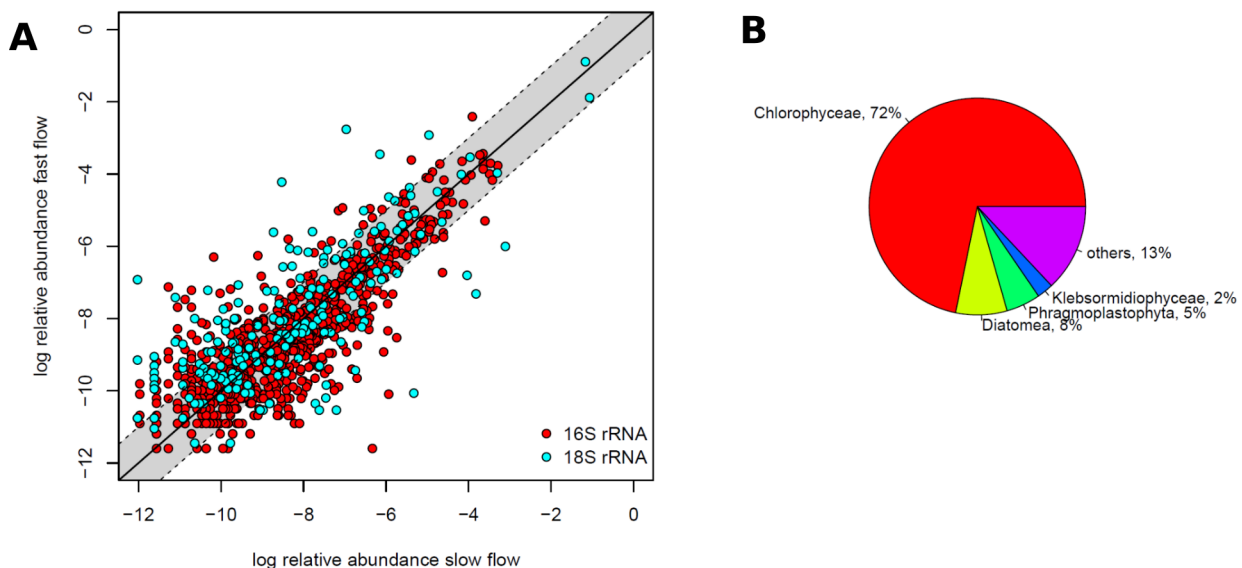
**Supplemental Figure S3. Community composition in experimental biofilms, Related to Figure 1.** Community composition did not differ between SFM and FFM morphotypes (A). Shown are average relative abundance (log) for 16S rRNA and 18S rRNA sequence variants for biofilms sampled from slow and fast flow areas. Only sequence variants that occurred in both morphotypes are shown (n_{16S} = 779, cumulative relative abundance: 96.9% of the entire 16S rRNA dataset; n_{18S} = 390, cumulative relative abundance of the entire 18S rRNA dataset: 98.3%). The 1:1 line (solid line) and the grey shaded area denoting ± 1 log units from the 1:1 line are shown for guidance. (B) Visual and microscopic inspection showed that biofilm biomass was dominated by phototrophic microorganisms. Refining the 18S rRNA gene dataset to include taxonomically resolved Archaeplastida, Stramopiles, Alveolates and Rhizaria (the three latter being combined to the supergroup SAR), we retained 173 sequence variants. Together, they represented 53.3% of relative read counts for the 18S rRNA dataset, with Ophistokonta and Amoebozoa representing another 44.8%. The phototrophic communities included 18 taxonomically resolved classes, which were dominated by Chlorophyceae (71.7% relative read counts), Diatomea (7.7%), and Zygnematophyceae (5.1%). Chlorophyceae included 13 distinct 18S rRNA sequence variants, however, across all samples, they were dominated by a single ASV (contributing to 95% of reads classified as Chlorophyceae). A blast search of this sequence resulted in hits to Scencedesmus sp. (blastn against nr/nt database, max score 695, E-value < 1e-179). Scenedesmus is a common, colony-forming (4 - 30 elongated cells laterally joined), non-motile and high-ligth adapted freshwater green algae (Chlorococcales), often found in stream biofilms (e.g. Pohlon et al., 2010; Sherwood, 2016), and can pioneer biofilm succession (Roeselers et al., 2007). The phototrophic biofilms were further composed of diverse Diatomea predominantely classified as Bacillariophytina (with 12 sequence variants and 5.2 out of 7.7% overall contribution of Diatomea to phototrophic community read counts) and Fragilariales (6 sequence variants and 2.4% out of 7.7% contribution). Both Bacillariophytina and Fragilariales are common in stream and river biofilms, where they often dominate carbon fixation (Burliga and Kociolek, 2016). Commonly described as diatoms, these taxa often assume a benthic livestyle in flowing waters, facilitated by fibrillar attachment structures (Wang et al., 2014) and the production of extracellular polymeric substances (EPS) which are released from the apical field of pennate diatoms. Mougeotia sp. (Phragmoplastophyta, Zygnematophyceae) is a cosmopolitan mat-forming freshwater algae and may occur in later stages of biofilm formation (Stelzer and Lamberti, 2001). Taken together, our experimental biofilms were composed of a diverse assemblage of common freshwater biofilm forming taxa, such as found in many streams and rivers.
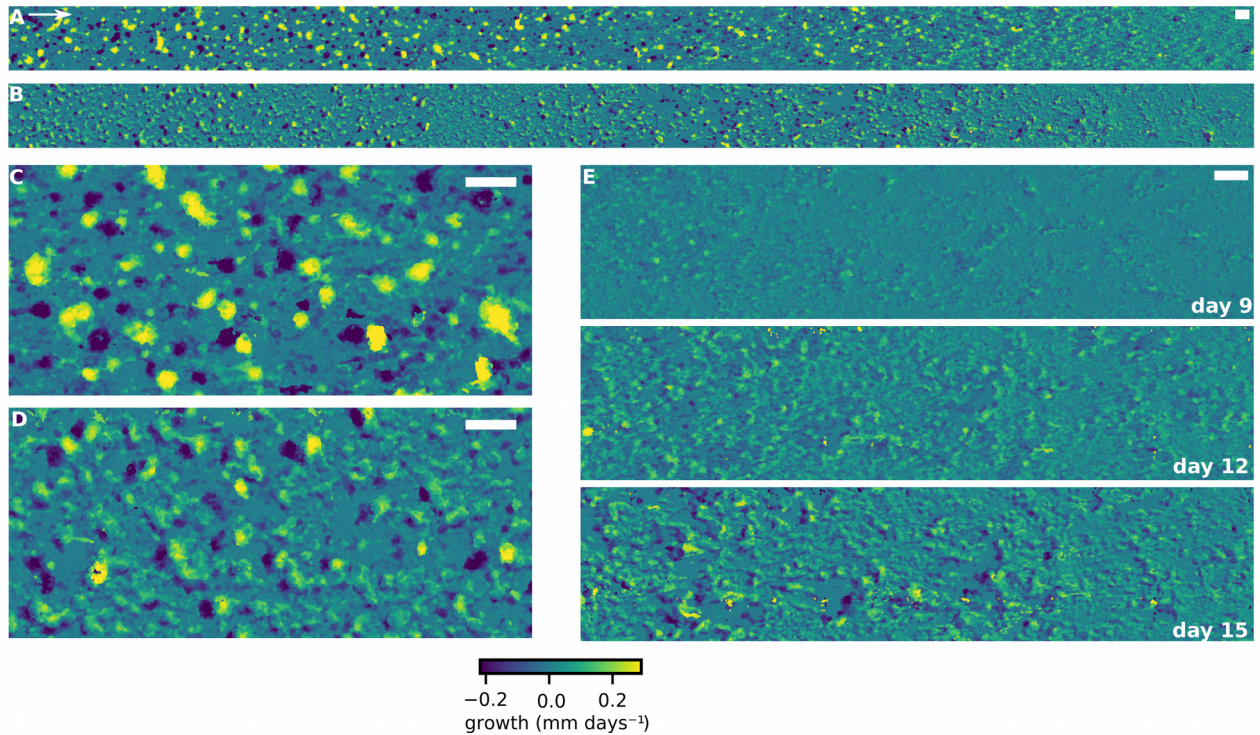
Supplemental Figure S4. Estimating displacement, Related to Figure 4. The OCT derived DEMs obtained at subsequent time points were subtracted to obtain the rate of increase in biofilm height per day. Panels A and C refer to flume II between day 12 and 15, while B and D to flume I between the same time-points. We attribute areas with negative accrual rates to displacement of biofilm clusters. Panel E shows the progressive enlargement of empty areas in the flow direction and the formation of structures resembling migratory ripples at the transition between the two morphotypes (time points are indicated). Scale-bars: 5 mm.
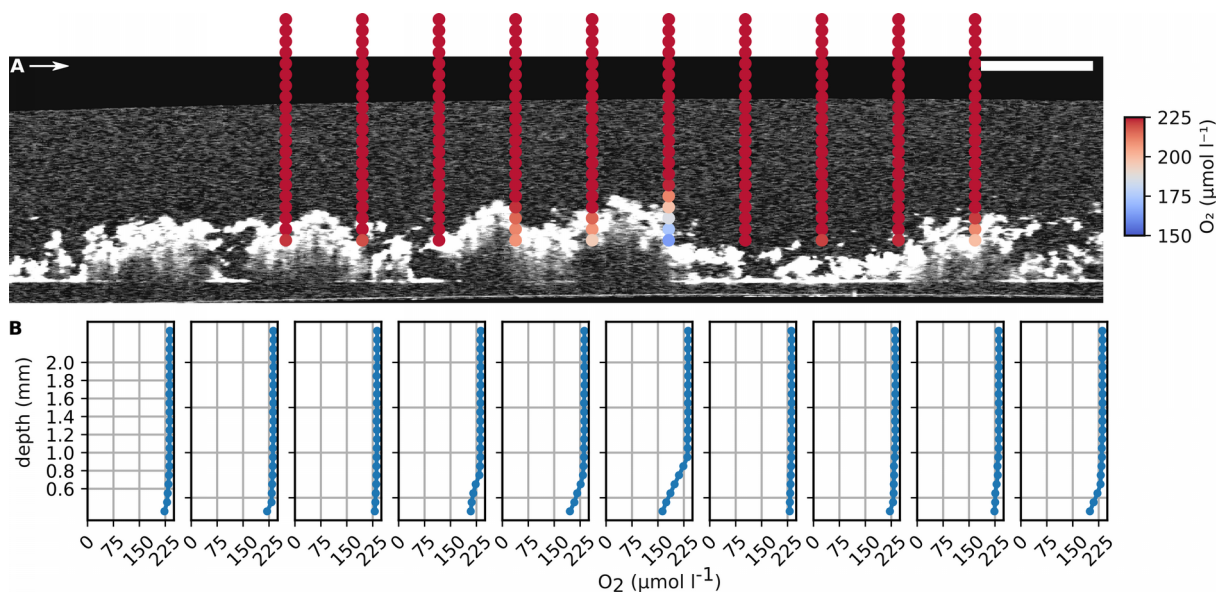
Supplemental Figure S5. Oxygen microprofiling, Related to Figure 5 and Figure 6. Shown are representative oxygen measurements within and around a biofilm structure (FFM) superimposed onto the respective OCT scan. Each point depicts the concentration of a single oxygen measurement in darkness (scale bar: 5 mm, arrow indicates the flow direction). The corresponding oxygen microprofiles are shown below. Note the absence of a diffusive boundary layer.
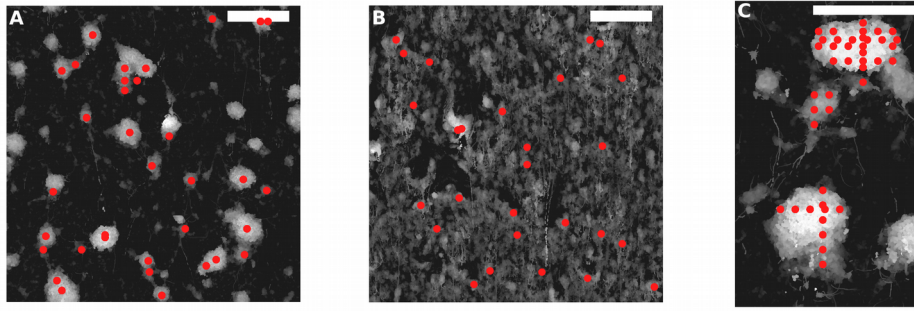
Supplemental Figure S6. Positions of the measured profiles, Related to Figure 6. To assess the spatial heterogeneity of the concentration of oxygen, we measured 35 and 27 oxygen profiles in both light and dark, for the slow flow morphotype (SFM) (A) and fast-flow morphotype (FFM) respectively (B). The locations of these profiles are indicated by the red dots. Further, we obtained 24 oxygen profiles in different positions within two clumps of the SFM, in dark conditions (C). Scale-bars are 5 mm.
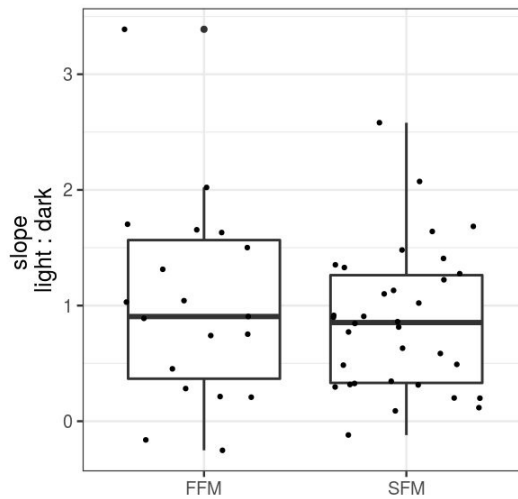
Supplemental Figure S7. Autotrophic and heterotrophic balance, Related to Figure 6. The ratio of the slope of the O_2 gradient below the biofilm surface (between 0.05 and 0.15 mm within the biofilm, light:dark) indicated a balance between heterotrophic and autotrophic aerial oxygen flux in SFM and FFM.

Transparent Methods

Flume experiments. Water from Lake Geneva was continuously filtered (nominal pore size 50 μm, FA 10 SX 50 ATLAS FILTRI) into a 1 m^3 reservoir and from there pumped into open-channel flumes. A constant flow rate (2.22×10^{-4} m^3 s^{-1}) was supplied using valves equipped with flow meters. Water was recirculated in a large reservoir, in which the water level was kept constant with a continuous inflow from the lake (8.3×10^{-6} m^3 s^{-1}). The total water volume in the flume was ~ 5.8×10^{-3} m^3, resulting in an average residence time of 26 s. Water temperature varied between 14.5°C and 15.5°C throughout the experiments, while pH oscillated between 7.16 and 7.55 (7.72 ± 0.30 [mean ± standard deviation]). Every 3 - 5 days, a water sample was filtered (0.22 μm polycarbonate filters, Isopore, Millipore) and analyzed by ion chromatography (Metrohm 930 Compact). Nitrate concentrations averaged 2.5 ± 0.4 mg l^{-1} and nitrite was below detection limit (< 0.05 mg l^{-1}). Further, total dissolved organic carbon (DOC) was quantified in filtered sample (pre-ashed GF/F, Whatman) using a TOC carbon analyzer (Sievers M9 TOC Analyser, GE). DOC varied between 872 and 3580 ppb, and averaged 1706 ± 731 ppb. Ammonia was quantified spectrophotometrically as described in (Taylor et al., 2007), and averaged 4.7 ± 0.9 μg l^{-1}. Soluble reactive phosphorous was quantified using the methylene blue method and averaged 2.0 ± 1.3 μg l^{-1}. Light (~13 W m^{-2}, JAZ spectrometer Ocean Optics) was provided for 12 hours per day using a combination of red and blue LEDs. The flumes were constructed from plexiglass with a funnel-like shape, imposing a gradient of flow velocity and bed shear stress on phototrophic biofilms. Flume width decreased gradually from 0.3 m to 0.05 m, with a slight curvature (**Supplementary Figure 1**). Average water depth was 0.022 m. The inflow was equipped with a round shaped adapter and a diffuser to minimize upstream turbulence. Prior to experiments, phototrophic biofilms growing continuously in the reservoir were harvested and disaggregated by shaking. The slurry was filtered using (41 μm nylon filter, Millipore) and diluted into 8 L of lake water. The biofilm slurry was then poured into the flumes and incubated for 12 hours without flow (under light). This seeding resulted in a thin layer of base biofilm evenly covering the flume bottom. After seeding, the flow was started and biofilm was allowed to grow without disturbance for 15 days.

Hydraulic gradient characterization. Mean flow velocity (u) and Reynolds number (R) were estimated from the flume geometry, the water depth (0.022 m), and discharge (2.22×10^{-4} m^3 s^{-1}) using formulas (1,2).

$$u = \frac{Q}{h \times w} \qquad (1)$$

$$R = \frac{Q}{v \times (2 \times h + w)} \qquad (2)$$

where v is the kinematic viscosity of water, Q is the discharge, w is the flume's width and h is the water depth.

The flow velocity within the open-channel flow chamber without biofilms was modeled using the geometrical design of the flume (Supplementary Figure 1). We used FLUENT (ANSYS R.19) to numerically solve a multiphase model (Volume of Fluid method), including 0.022 m water phase at the bottom of the flume, and a 0.018 m thick volume of air on top. We used the Reynolds-averaged Navier-Stokes approach, with a no slip-boundary condition on the plexiglass surface. An SST k-ω turbulence model (Menter, 1993), that is a two-equation eddy-viscosity model, was used to model turbulence. SST k-ω ensures simulation accuracy across the flow field by employing k-ω turbulence model in the regions near the wall and k-ε in other regions. The flow was generated by a pressure gradient between inlet and outlet. In order to resemble the flume flow field, boundary conditions were set similar to the flume operating conditions where the inlet discharge was 2.22×10^{-4} m^3 s^{-1}. The

results of the simulation were used to estimate the velocity magnitude in every point, calculated as the sum of the x- y- and z- vector components of velocity.

Bed shear stress was estimated as

$$\tau_s = \mu \left(\frac{du}{dy} \right)_{y=0}$$

where μ is the dynamic viscosity of water at 15°C.

OCT positioning and imaging. We used a spectral domain optical coherence tomograph (GANYMEDE, Thorlabs GmbH, Germany) centered at 930 nm and equipped with an immersion adapter. OCT datasets were acquired by averaging 3 A-scans and had a resolution of 40 µm in x and y and 2.18 µm in z direction, covering a volume of 10 mm × 10 mm × 2.23 mm. We mounted the OCT probe on a precision positioning device (STEPCRAFT, 30 µm precision in x,y), as described previously (Depetris et al., 2019). Automatic positioning and OCT scan acquisition allowed us to obtain 66 × 3 OCT scans in a mosaic pattern (overlap was set to 30 % of the field of view). The final stitched OCT covered a total field of 0.040 × 0.0024 m. Further, higher resolution (11 µm x, y and 2.18 µm z) images in tiled patterns of 3 × 3 were taken at the two extremes of the velocity gradient. Biofilms were imaged every 3 days.

OCT scan processing and analysis. OCT scans were corrected for the lateral distortion using a custom made algorithm (Depetris et al., 2019). Then, OCT scans were binarized and the thickness of the biofilm at each position encoded in a digital elevation model (DEM). DEMs were cropped ~ 50 µm above the plexiglass surface; this represents the minimum height of structures considered in this work. Shorter structures were disregarded, in order to avoid fine irregularities of the plexiglass. Elevation maps were then stitched and denoised with a median filter. Biovolume was estimated as the volume beneath the biofilm surface, (*i.e.,* the sum of all pixels values in the DEM). This was supported by visual inspection of the OCT images, which did not reveal the presence of voids below the biofilm surface. Biofilm accrual rate over 3 days was calculated as the difference in biovolume between subsequent time-points, divided by the time lag (3 days). Biofilm maximum thickness was calculated as the 0.95 percentile of the height distribution; coverage was calculated as the percentage of the pixels within a DEM with values greater than zero. Biofilm solids hold-up was calculated as described by Picioreanu et al. (Picioreanu et al., 1998), as the ratio between biofilm volume and the volume of a parallelepiped with a basal area equal to the substrate's surface area and height equal to the maximum biofilm height. Porosity was them calculated as 1 - biofilm solids hold-up. Textural correlation was calculated from the gray-level co-occurrence matrix (Haralick et al., 1973) using the *scikit-image* package GLCM Texture Features, with distance = 200 µm and angle = 0°. Setting the distance parameter from 0 to 4000 µm and angles 0°, 90°, 180° did not qualitatively change the results. A square window of 0.024 m edge was moved along the stitched DEM in steps of 4 mm. For the fragmented regression analysis, we applied the Davies test to test for the presence of a breakpoint (function *davies.test* in R). Then, the position of the breakpoint and the slopes of the two contrasting trends were estimated using the '*segmented'* R package using 0.11 Pa as a starting value (Muggeo, 2008). The significance of the trend in biofilm architectural features with increasing shear was tested within the two fragments (or on the entire dataset when the Davies test did not evidence a significant breakpoint) using a modified version of the Mann Kendall test for autocorrelated data (Hamed and Ramachandra Rao, 1998), using the R function *mmkh* (from the package '*modifiedmk'*). Finally, in the absence of a significant breakpoint, the slope of the significant trends was estimated with a linear model. For these analyses, the dataset was reduced to include only non-overlapping windows and avoid excessive spatial autocorrelation. Linear regressions for the relationship between volume, height and coverage were also computed using R (R Core Team, 2020). Image processing and analyses were done using Python, NumPy, scikit-image package when not stated otherwise. Jupyter notebook are available [here](#). To analyze biofilm morphogenesis, we utilized higher resolution OCT scans (11.1 µm, 11.1 µm, 2.18 µm in x, y, z),

which were processed analogously to the lower resolution counterparts. Volume, height, coverage and textural correlation were calculated as before. To segment troughs, clusters and valleys, we applied a gaussian filter with sigma 2.2 mm and selected areas that were 2 times taller than the filtered image as clusters, and 0.5 times lower as troughs. Segmentation parameters were chosen on the basis of a visual checks. The shape of individual clusters was analyzed using the *regionprops* function of the *scikit-image* package. Volume was calculated as the sum of pixels in the portion of the DEM containing the cluster of interest. The horizontal aspect ratio was calculated as the ratio between the major and minor axes of the ellipse that has the same normalized second central moment as the region basal area. Orientation represents the angle of the major axis with respect to the flow direction. The vertical aspect ratio was calculated as the ratio between cluster height and the square root of its basal area. Displaced volume and coverage were calculated by subtracting subsequent DEMs in the time series and selecting areas with negative values.

Fluid dynamics simulation around two idealized biofilm clusters. We simulate the 3-dimensional laminar stationary flow around two idealized biofilm clusters using Comsol Multiphysics 5.4. The computational domain represents a sub-region from our experiment, and it consists of a rectangular block with dimensions L_x = 16.5 mm, L_y = 7.5 mm and L_z = 4.5 mm. A right-handed co-ordinate system is centered at the center of the bottom surface. The idealized bio-film clusters are modeled as two impermeable rigid vertical structures each comprising of a circular cylinder (radius = 1.25 mm, height = 1 mm) capped with a truncated hemisphere of radius 2.15 mm. The two cylinders are symmetrically located on the bottom surface along the streamwise (x-axis) direction with center-center distance of 4 mm. We provide an inlet flow condition of uniform mass flux of 0.2 g s^{-1} chosen strategically based on experimental conditions. The boundary conditions are applied such that each boundary represents that of a sub-volume in the experimental field; no-slip on the bottom surface including the surface of each cluster, open-flow condition (with zero viscous stress) on the top surface, and periodic boundary conditions are applied on the two side surfaces. We use adaptive tetrahedral mesh with minimum element size of 8 microns near each rigid surface, such that the boundary layers are well resolved.

Microsensor measurements and microprofile analysis. Oxygen concentration microprofiles were measured with a fast-response Clark-type O_2 microsensor (tip diameter 10 µm, OX-10, Unisense A/S, Aarhus, Denmark), with steps of 50 µm. The microelectrode was calibrated in air-saturated water and anoxic sodium ascorbate solution. The microsensor was vertically mounted on a motorized micromanipulator (Unisense A/S) and connected to a microsensor multimeter (Unisense A/S). Data acquisition and micromanipulator positioning were controlled by a dedicated software (Sensor TracePro, Unisense A/S). The positioning the tip of the microsensor was monitored with an endoscope. Profiles were taken in light and dark, with a lag period of 1 hour after changing light condition, between 15 and 19 days of growth, only for flume II. Difference of oxygen concentration in the light and dark were calculated for each point and used as a measure of diel variability in oxygen micro-niches. The pooled oxygen concentration distributions (within the biofilm) under light, dark or their difference were significantly not normal (Shapiro test, p-value < 0.01 for each), and they differed significantly for the two morphotypes (Mann–Whitney test, p-value < 0.01 for each). We used the robust Brown-Forsythe Levene-type test from the *lawstat* R package, to test for differences in variance of FFM and SFM. We compared oxygen concentration distributions at comparable depth within the biofilm in the SFM and FFM, in both light conditions, using the unpaired samples t-test with uneven variances. For this analysis, measurement points were pooled in steps of 0.1 mm depth, to account for the uncertainty in the position of the biofilm surface. Distance from clump walls was calculated using the Euclidean distance transform function (from the *scipy.ndimage* package) applied to the binarized DEM. The ratio of the oxygen gradient below the biofilm surface (between 0.05 mm and 0.2 mm) in light and dark (for each profile) was used as an estimate of the relative contribution of photosynthesis and respiration to the net oxygen flux in that point. Also in this case, we used a Welch's two-samples t-test to test for differences between the SFM and FFM.

DNA extraction, sequencing and bioinformatics. We sampled biofilms at the two extremes of the morphological gradient using sterile swabs. Samples were flash frozen at - 80°C and subsequently DNA was isolated using the DNeasy Power Soil kit (QIAGEN). The 16S and 18S rRNA genes were amplified using PCR with the 341f (5'CCTACGGGNGGCWGCAG-3′) and 785r (5′-GACTACHVGGGTATCTAAKCC-3′; Klindworth et al. 2012) and TAReuk454FWD1 (5'-TCGTCGGCAGCGTCAGATGTGTATAAGAGACAG-3') and TAReukREV3 (5'-GTCTCGTGGGCTCGGAGATGTGTATAAGAGACA-3'; Stoeck et al., 2010) primer pairs, for prokaryotic and eukaryotic community members, respectively. Sequencing libraries were prepared using the Nextera XT kit (Illumina), equimolar pooled and sequenced on a 300 bp paired-end MiSeq (Illumina) run at the Lausanne Genomic Technology Facility (LGTF). Sequencing adapters were clipped from the raw reads which were subsequently denoised and clustered into Amplicon Sequence Variants (ASV) using dada2 (vers. 1.14) (Callahan et al., 2016) as implemented in qiime2 (Bolyen et al., 2019). After taxonomic assignment, autotrophic community members were extracted from the 18S dataset. Analysis of similarity (anosim) was performed on Bray-Curtis distance matrices using the R package *vegan* (Oksanen et al. 2019).

References

Bolyen, E., Rideout, J.R., Dillon, M.R., Bokulich, N.A., Abnet, C.C., Al-Ghalith, G.A., Alexander, H., Alm, E.J., Arumugam, M., Asnicar, F., et al. (2019). Reproducible, interactive, scalable and extensible microbiome data science using QIIME 2. Nat. Biotechnol. *37*, 852–857.

Burliga, A.L., and Kociolek, J.P. (2016). Diatoms (Bacillariophyta) in Rivers. In River Algae, (Cham: Springer International Publishing), pp. 93–128.

Callahan, B.J., McMurdie, P.J., Rosen, M.J., Han, A.W., Johnson, A.J.A., and Holmes, S.P. (2016). DADA2: High-resolution sample inference from Illumina amplicon data. Nat. Methods *13*, 581–583.

Depetris, A., Wiedmer, A., Wagner, M., Schäfer, S., Battin, T.J., and Peter, H. (2019). Automated 3D Optical Coherence Tomography to Elucidate Biofilm Morphogenesis Over Large Spatial Scales. J. Vis. Exp. 1–9.

Hamed, K.H., and Ramachandra Rao, A. (1998). A modified Mann-Kendall trend test for autocorrelated data. J. Hydrol. *204*, 182–196.

Haralick, R.M., Shanmugam, K., and Dinstein, I. (1973). Textural Features for Image Classification. IEEE Trans. Syst. Man. Cybern. *SMC-3*, 610–621.

Menter, F.R. (1993). Zonal two equation kappa-omega turbulence models for aerodynamic flows (Provided by the SAO/NASA Astrophysics Data System).

Muggeo, V.M.R. (2008). segmented: An R package to Fit Regression Models with Broken-Line Relationships. R NEWS *8/1*, 20--25.

Picioreanu, C., van Loosdrecht, M.C.M., and Heijnen, J.J. (1998). Mathematical modeling of biofilm structure with a hybrid differential-discrete cellular automaton approach. Biotechnol. Bioeng. *58*, 101–116.

Pohlon, E., Marxsen, J., and Küsel, K. (2010). Pioneering bacterial and algal communities and potential extracellular enzyme activities of stream biofilms. FEMS Microbiol. Ecol. *71*, 364–373.

R Core Team (2020). R: A Language and Environment for Statistical Computing.

Roeselers, G., Van Loosdrecht, M.C.M., and Muyzer, G. (2007). Heterotrophic pioneers facilitate phototrophic biofilm development. Microb. Ecol. *54*, 578–585.

Schindelin, J., Arganda-Carreras, I., and Frise, E. (2012). Fiji: an open-source platform for biological-image analysis. Nat. Methods.

Sherwood, A.R. (2016). Green Algae (Chlorophyta and Streptophyta) in Rivers. In River Algae, (Cham: Springer International Publishing), pp. 35–63.

Stelzer, R.S., and Lamberti, G.A. (2001). Effects of N : P ratio and total nutrient concentration on stream periphyton community structure, biomass, and elemental composition. Limnol. Oceanogr. *46*, 356–367.

Stoeck, T., Bass, D., Nebel, M., Christen, R., Jones, M.D.M., Breiner, H.-W., and Richards, T.A. (2010). Multiple marker parallel tag environmental DNA sequencing reveals a highly complex eukaryotic community in marine anoxic water. Mol. Ecol. *19*, 21–31.

Taylor, B.W., Keep, C.F., Hall, R.O., Koch, B.J., Tronstad, L.M., Flecker, A.S., and Ulseth, A.J. (2007). Improving the fluorometric ammonium method: Matrix effects, background fluorescence, and standard additions. J. North Am. Benthol. Soc.

Wang, Q., Hamilton, P.B., and Kang, F. (2014). Observations on attachment strategies of periphytic diatoms in changing lotic systems (Ottawa, Canada). Nov. Hedwigia *99*, 239–253.

Oksanen, J., Blanchet, F.G., Friendly, M., Kindt, R., Legendre, P., McGlinn, D., Minchin, P.R., O'hara, R.B., Simpson, G.L., Solymos, P. and Stevens, M.H.H., 2016. vegan: Community Ecology Package. R package version 2.4-3. *Vienna: R Foundation for Statistical Computing.*